CAPITAL UNIVERSITY OF SCIENCE AND TECHNOLOGY, ISLAMABAD

Machine Learning based Laser-Powder Bed Fusion Process Parameterization for Nitinol

by

Muhammad Hamza Javed

A thesis submitted in partial fulfillment for the
degree of Master of Science

in the
Faculty of Engineering
Department of Mechanical Engineering

2026

Copyright © 2026 by Muhammad Hamza Javed

All rights reserved. No part of this thesis may be reproduced, distributed, or transmitted in any form or by any means, including photocopying, recording, or other electronic or mechanical methods, by any information storage and retrieval system without the prior written permission of the author.

CERTIFICATE OF APPROVAL

Machine Learning based Laser-Powder Bed Fusion Process Parameterization for Nitinol

by

Muhammad Hamza Javed

(MME231001)

THESIS EXAMINING COMMITTEE

S. No.	Examiner	Name	Organization
(a)	External Examiner	Dr. Muhammad Jawad Khan	NUST, Islamabad
(b)	Internal Examiner	Dr. Manzar Masud	CUST, Islamabad

Dr. Shummaila Rasheed
Thesis Supervisor
April, 2026

Dr. M. Mahabat Khan
Head
Dept. of Mechanical Engineering
April, 2026

Dr. Imtiaz Ahmad Taj
Dean
Faculty of Engineering
April, 2026

Author's Declaration

I, **Muhammad Hamza Javed** hereby state that my MS thesis titled "**Machine Learning based Laser-Powder Bed Fusion Process Parameterization for Nitinol**" is my own work and has not been submitted previously by me for taking any degree from Capital University of Science and Technology, Islamabad or anywhere else in the country/abroad.

At any time if my statement is found to be incorrect even after my graduation, the University has the right to withdraw my MS Degree.

M. Hamza Javed

(Muhammad Hamza Javed)
Registration No: MME231001

Plagiarism Undertaking

I solemnly declare that research work presented in this thesis titled "**Machine Learning based Laser-Powder Bed Fusion Process Parameterization for Nitinol**" is solely my research work with no significant contribution from any other person. Small contribution/help wherever taken has been duly acknowledged and that complete thesis has been written by me.

I understand the zero tolerance policy of the HEC and Capital University of Science and Technology towards plagiarism. Therefore, I as an author of the above titled thesis declare that no portion of my thesis has been plagiarized and any material used as reference is properly referred/cited.

I undertake that if I am found guilty of any formal plagiarism in the above titled thesis even after award of MS Degree, the University reserves the right to withdraw/revoke my MS degree and that HEC and the University have the right to publish my name on the HEC/University website on which names of students are placed who submitted plagiarized work.

M. Hamza Javed

(Muhammad Hamza Javed)
Registration No: MME231001

Acknowledgement

All praise and gratitude are due to **Allah Almighty**, whose infinite mercy, blessings, and guidance granted me the strength, perseverance, and resolve to complete this thesis. Nothing is possible without His will. I also extend my deepest salutations and peace upon the beloved **Prophet Muhammad (PBUH)**, whose exemplary life and teachings continue to serve as a profound source of guidance and inspiration.

I express my sincere and heartfelt gratitude to my respected supervisor, **Dr. Shummaila Rasheed**, for her exceptional guidance, continuous support, and invaluable mentorship throughout this research. Her insightful feedback, constructive suggestions, and consistent encouragement played a pivotal role in shaping this study and strengthening my academic confidence. Her patience, dedication, and commitment to scholarly excellence have been truly motivating, and this work would not have been possible without her distinguished supervision.

To all those who supported and encouraged me throughout this journey, I remain deeply thankful and sincerely appreciative.

(Muhammad Hamza Javed)

Abstract

This thesis proposes an ANN-based framework for interpreting Laser Powder Bed Fusion (L-PBF) parameter effects in NiTi alloy by linking model prediction error to recalculated volumetric energy density. The main contribution of the study is not only the prediction of relative density, but the integration of ANN error into an adjusted VED/BED descriptor to assess how prediction uncertainty influences energy-based process interpretation. The analysis was based on a literature-derived dataset extracted from Obeidi, consisting of 27 unique combinations of laser power, scanning speed, and pulse frequency, with experimentally measured relative density reported for 40 μm and 80 μm layer-thickness conditions. These were analyzed as two separate 27-sample datasets using three ANN training algorithms in MATLAB: Levenberg–Marquardt (LM), Bayesian Regularization (BR), and Scaled Conjugate Gradient (SCG). The results showed that LM provided the strongest relative-density prediction performance overall, while the lowest VED deviation was obtained with SCG for the 40 μm dataset and with BR for the 80 μm dataset. Comparative deviation analysis further indicated that the 80 μm condition was more sensitive to ANN prediction error than the 40 μm condition. Response-surface and Pareto analyses showed that pulse frequency was the dominant factor affecting relative density, whereas scanning speed and laser power had secondary effects within the investigated range. Overall, the study demonstrates that incorporating ANN prediction error into VED/BED analysis provides a more informative basis for L-PBF process assessment than using a static energy descriptor alone.

Contents

List of Figures

List of Tables

Abbreviations

AM	Additive Manufacturing
ANN	Artificial Neural Network
BED	Bulk Energy Density
BR	Bayesian Regularisation (training algorithm)
CAD	Computer-Aided Design
CNN	Convolutional Neural Network
DED	Directed Energy Deposition
DoE	Design of Experiments
DSC	Differential Scanning Calorimetry
GBR	Gradient Boosting Regression
GPR	Gaussian Process Regression
KNN	k-Nearest Neighbours
LM	Levenberg–Marquardt (training algorithm)
L-PBF	Laser Powder Bed Fusion
ML	Machine Learning
MSE	Mean Squared Error
NiTi	Nickel–Titanium Shape Memory Alloy
PBF	Powder Bed Fusion
$\mathbf{R}^2$	Coefficient of Determination
RFR	Random Forest Regression
RMSE	Root Mean Squared Error
SCG	Scaled Conjugate Gradient (training algorithm)
SEM	Scanning Electron Microscopy
SVR	Support Vector Regression

VED	Volumetric Energy Density
XCT	X-ray Computed Tomography
XRD	X-ray Diffraction

Symbols

P	Laser power	W
v	Scanning speed	mm·s^{-1}
h	Hatch spacing	mm
t	Layer thickness	mm
ρ_r	Relative density	%
VED	Volumetric energy density	J·mm^{-3}
BED	Bulk energy density	J·mm^{-3}
n	Number of samples / data points	–
y_i	Experimental (target) value for sample i	– or %
$\hat{y}_i$	ANN-predicted value for sample i	– or %
MSE	Mean squared error	unit of y^2
R	Correlation coefficient	–
MSE_w	Error-weighting function in adjusted VED	–
VED_{ANN}	ANN-adjusted volumetric energy density	J·mm^{-3}

Chapter 1

Introduction

Additive manufacturing (also known as AM) has experienced intense growth in the past few years because of the increased adoption rate of the flexible production process [1]. Additive manufacturing makes it easy to produce complex structures. In fact, it reduces material waste because customized designs cannot be produced using subtractive techniques. The layer-manufacturing method has changed the way products are produced because process control using data is now very important for achieving process quality.

1.1 Additive Manufacturing

Additive manufacturing describes a set of technologies that use layered deposition to create a three-dimensional object [2]. These technologies build products directly from computer-aided design models. Seven types of AM, according to ISO/ASTM 52900, include the following benefits that give these technologies an advantage over subtractive or formative manufacturing techniques: a low volume of wasted material, flexibility to design the internal architecture of a product, and the ability to manufacture customized parts [3]. Three major AM process categories are illustrated in Figure 1.1.

1.1.1 Material Extrusion

Material extrusion technologies use the nozzle to extrude molten, semi-molten materials for the creation of layers [4]. By far, the most widely known technology comes in the form of Fused Deposition Modeling, which commonly involves the use of thermoplastics (Figure 1.1).

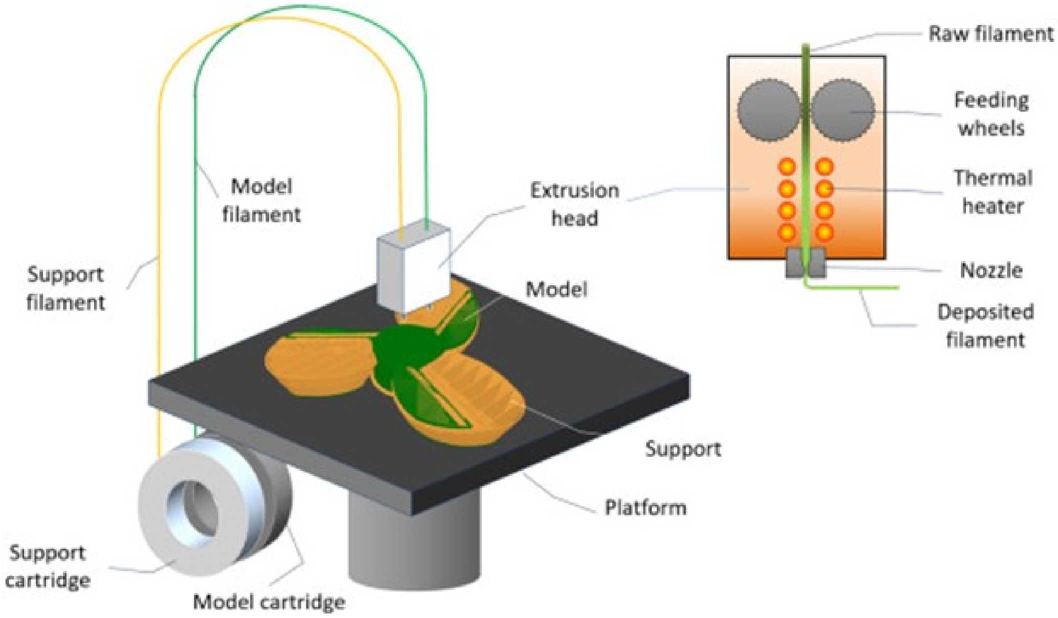

Figure 1.1: Schematic of the material extrusion process showing filament feeding, heating, and layer-by-layer deposition through a nozzle Source [5]

1.1.2 Vat Photopolymerization

Vat photopolymerization is a process of selectively curing a liquid resin contained in a vat using a light source (UV laser or projector). Stereolithography (SLA) is a prototypical example of vat photopolymerization (Figure 1.2). It provides a high-quality surface finish and is ideal for models and dental applications [6].

1.1.3 Powder Bed Fusion

In Powder Bed Fusion (PBF), thin layers of powder material are laid down and selectively melted with the help of a thermal energy source (laser or electron beam) (Figure 1.3). This category allows the creation of parts with high densities from

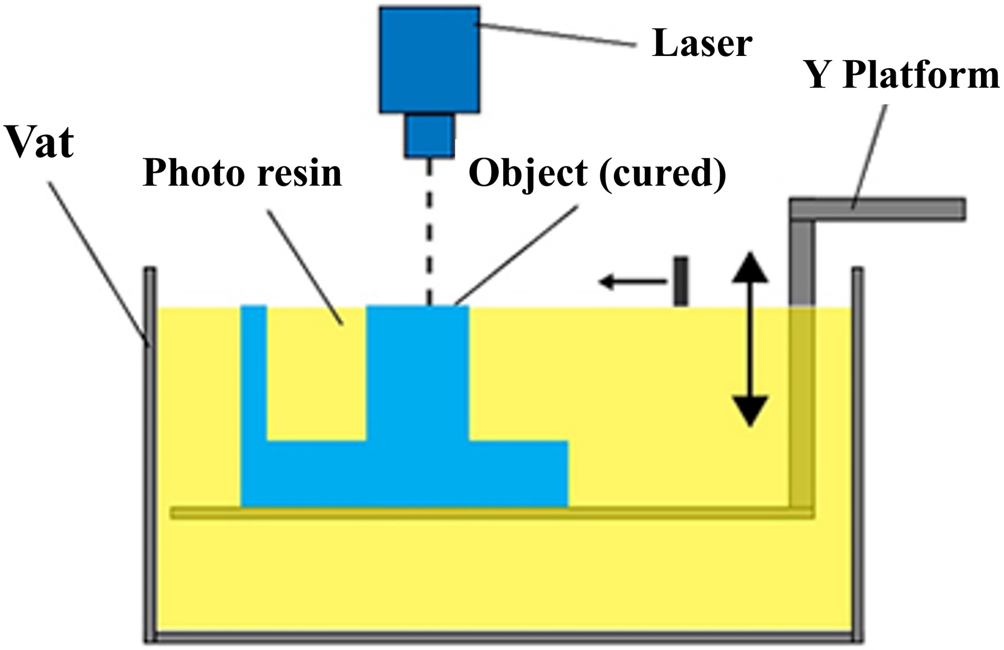

FIGURE 1.2: Schematic of vat photopolymerization showing selective laser curing of liquid resin layer by layer. Source [7]

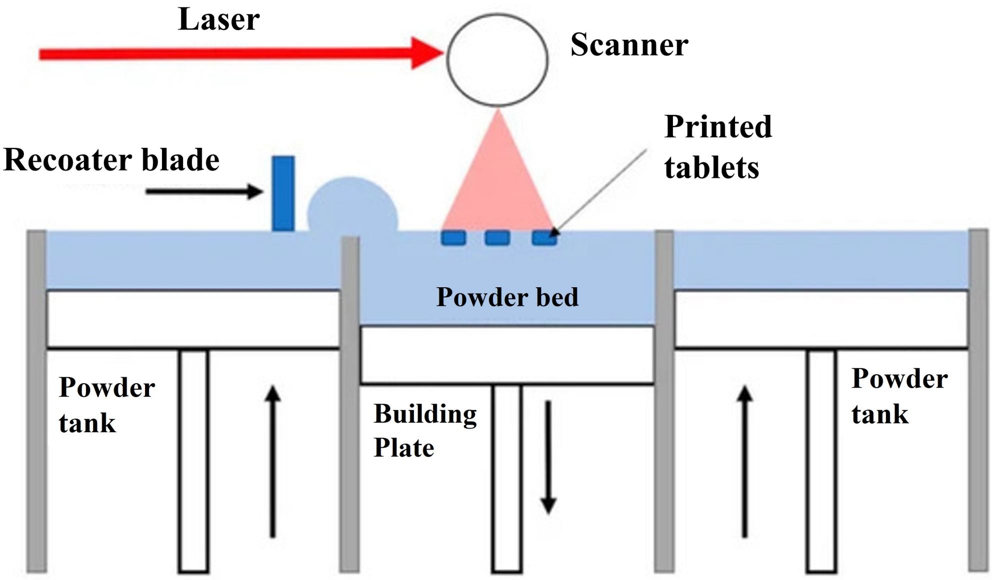

FIGURE 1.3: Powder Bed Fusion (PBF): powder is spread by a roller, selectively melted by a laser, and the build platform lowers for the next layer. Source [8]

polymers, metals, and ceramics, and is useful for the creation of functional parts with defined microstructures [8].

This study investigates the influence of key Laser Powder Bed Fusion (L-PBF) process parameters on the densification behaviour of NiTi alloys. Using a data-driven framework, it examines the relationships between selected processing conditions and relative density to support improved understanding and optimization of the L-PBF process.

1.2 What is Laser Powder Bed Fusion

L-PBF is a cutting-edge method for making metal parts that uses a high-energy laser beam to melt metallic powder in layers to create three-dimensional parts, as shown in Figure 1.4. Using a recoater blade or roller, the first step is to deposit a thin, even layer of metal powder over the build platform [9]. A focused laser beam then scans the part's cross-sectional shape, melting and fusing powder particles in specific areas based on the computer design. The cycle starts over again once the layer hardens. The build platform lowers, a fresh powder layer is added, and the process continues until the whole component is made. Because it heats up and cools down quickly in small areas, L-PBF can achieve outstanding geometrical accuracy, tight dimensional tolerances, and controlled microstructures [10]. These traits make it a popular choice for high-value functional parts where performance, weight reduction, and complex shapes are essential. The approach enables the creation of internal channels, lattice structures, and topologically optimized designs that can't be produced using traditional subtractive or formative production methods [11].

The quality of a part made with L-PBF depends a lot on how you choose and use process factors, including laser power, scanning speed, hatch spacing, layer thickness, and scan strategy. These factors directly affect the stability of the melt pool, the temperature gradients, the cooling rates, and the subsequent microstructural changes. Choosing the wrong parameters can lead to problems such as porosity, balling, incomplete melting, microcracks, and compositional changes [13]. So, it is still essential to understand and improve these characteristics to get high density, the proper mechanical performance, and consistent output. L-PBF works with a wide range of engineering alloys, including titanium alloys, nickel-based superalloys, aluminum alloys, and shape-memory alloys such as NiTi. Ongoing improvements in powder metallurgy and process monitoring have made materials

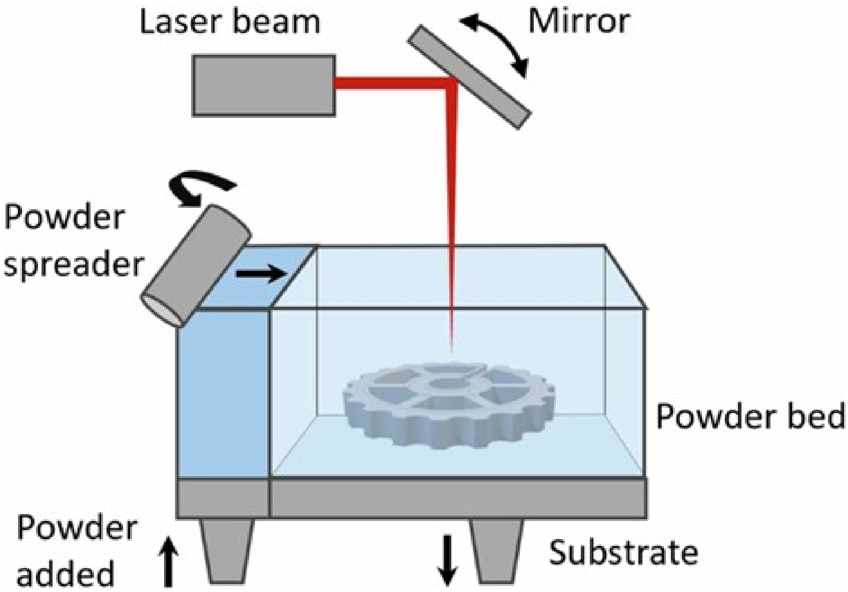

Figure 1.4: Schematic illustration of the L-PBF process, showing the laser scanning, powder deposition system, melt pool formation, and consolidation of successive layers to build the part geometry. Source: [12]

even more reliable and made L-PBF more widely used in industry. L-PBF is one of the most studied and widely used metal additive manufacturing technologies in industry because it can be applied to many different applications. It is the basis for lightweight structural design, tailored implants, and high-temperature-resistant aerospace parts [14].

1.2.1 Applications for Laser Powder Bed Fusion

Figure 1.5 shows the main industrial sectors that use L-PBF extensively to produce high-performance metal parts. The applications listed demonstrate that L-PBF can produce parts with complex shapes, built-in features, and customized mechanical properties. These benefits make the method a good fit for businesses where lowering weight, improving structural efficiency, and making things to order are essential [15].

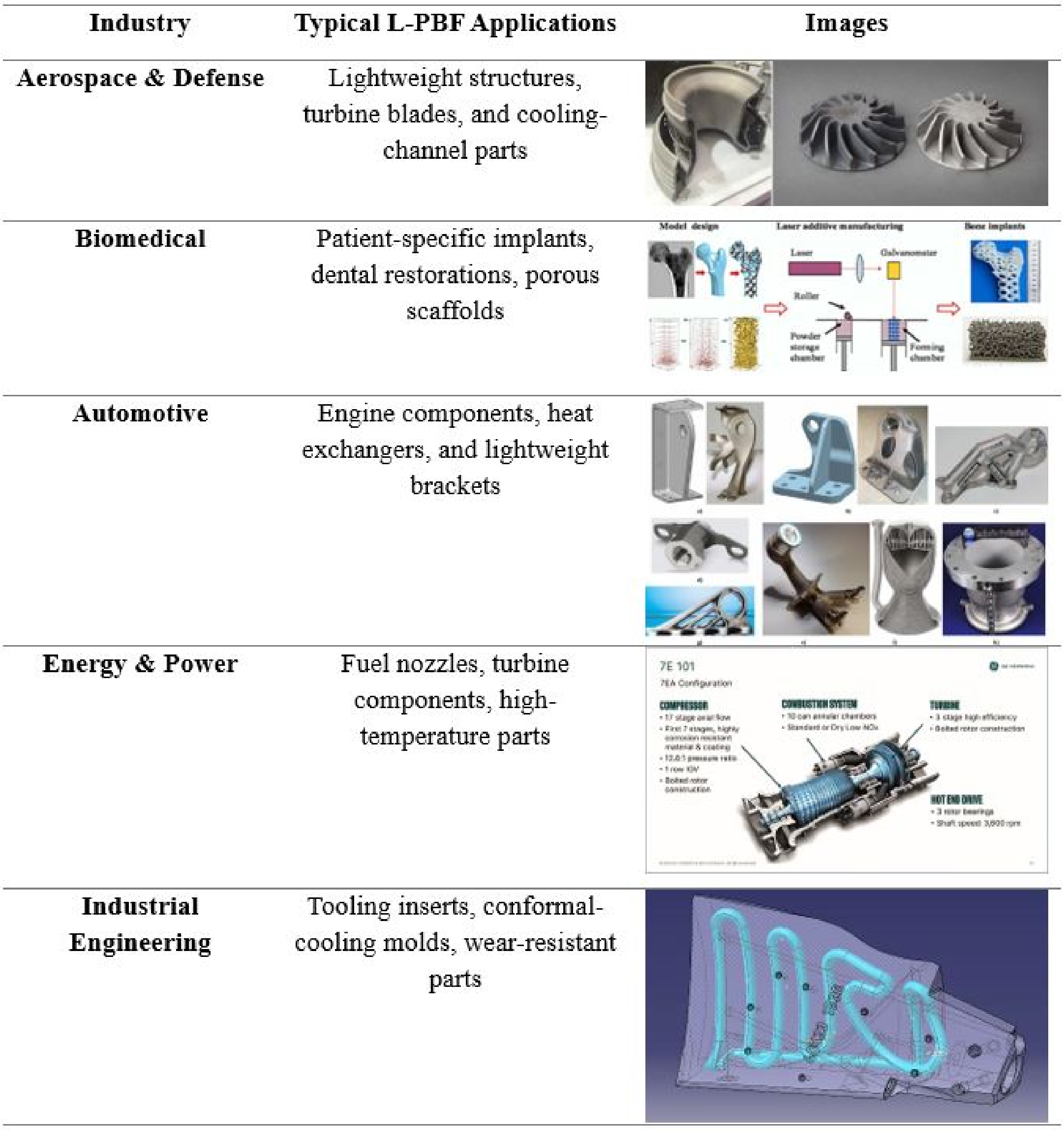

Industry	Typical L-PBF Applications	Images
Aerospace & Defense	Lightweight structures, turbine blades, and cooling-channel parts	
Biomedical	Patient-specific implants, dental restorations, porous scaffolds	
Automotive	Engine components, heat exchangers, and lightweight brackets	
Energy & Power	Fuel nozzles, turbine components, high-temperature parts	
Industrial Engineering	Tooling inserts, conformal-cooling molds, wear-resistant parts	

Figure 1.5: Key Applications of L-PBF [16–18]

1.3 Critical Process Parameters in Laser Powder Bed Fusion

In L-PBF, critical process parameters are the set of printing factors that can be controlled and directly affect thermal behavior, melt-pool stability, microstructural development, and the ultimate quality of the part. These settings control how much energy is applied to the powder bed, how the molten pool forms and hardens, and whether the process produces dense, defect-free parts. L-PBF exhibits fast heating and cooling cycles and complex thermal gradients. This means that even tiny changes in these settings can make significant changes in porosity, dimensional accuracy, surface polish, and mechanical performance [19, 20]. To make sure that metal additive manufacturing produces dependable, reproducible, and high-quality products, it is crucial to understand and improve these factors. The primary critical parameters in L-PBF include the following:

1.3.1 Laser Power

Laser power is the amount of energy the laser emits per unit of time. It is one of the main factors that cause melt pools. More powerful lasers raise the peak temperature, the depth of the melt pool, and the amount of powder that sticks together. But too much power can cause keyholing, the evaporation of alloying elements, spatter, and instability in the molten pool (Figure 1.6). On the other hand, insufficient power can lead to flaws in fusion and weak bonding between layers. So, choosing the right laser power is essential to ensure the whole thing melts without causing thermal flaws [21].

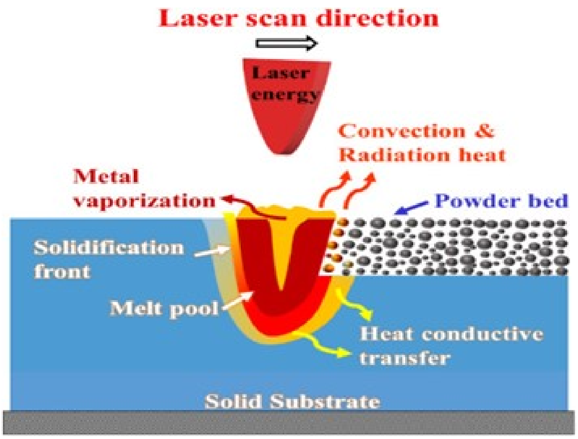

FIGURE 1.6: Effect of laser power on melt pool formation in L-PBF. Insufficient laser power results in lack-of-fusion defects, optimal power produces a stable melt pool with good interlayer bonding, while excessive laser power leads to keyholing. Source [22]

1.3.2 Scanning Speed

Scanning speed is the rate at which the laser traverses the powder bed and directly influences the energy input per unit length as well as the time available for melting. As illustrated in Figure A.1(a), increasing the scanning speed reduces the local energy supplied to the material, which can result in shallow melt pools and lack-of-fusion defects [23]. In contrast, excessively low scanning speeds increase heat accumulation and may promote overheating, balling, and microstructural coarsening, as schematically shown in Figure A.1(b). Therefore, an optimum scanning speed is required to maintain a stable melt pool geometry and ensure consistent track formation.

1.3.3 Hatch Spacing

The space between two laser scan tracks is called hatch spacing. It tells you how much the melt pools next to each other overlap. If the hatch spacing is too wide, the overlap is reduced, leaving areas that aren't melted, porosity increases, and density decreases. Too little space between them leads to excessive remelting, heat buildup, and distortion (Figure A.1). Proper hatch spacing ensures that the tracks join and consolidate evenly, improving density and mechanical stability [24].

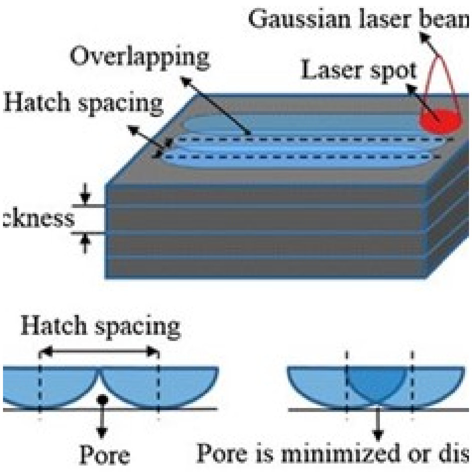

Figure 1.7: Schematic illustration of hatch spacing effects on scan track overlap and porosity formation in LPBF fusion. Source [24]

1.3.4 Layer Thickness

Layer thickness refers to the height of each new powder layer deposited on the build platform. Thin layers typically result in higher accuracy, finer microstructures, and improved surface quality. However, they increase building time. Thicker layers accelerate production but require higher energy input to ensure complete melting. If energy is insufficient, defects such as incomplete fusion may form (Figure 1 8). Layer thickness must therefore be balanced against productivity and part quality requirements.

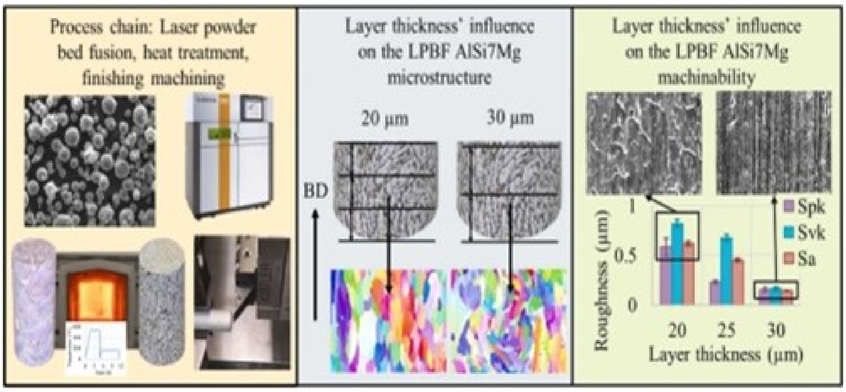

FIGURE 1.8: Effect of layer thickness on laser penetration depth and interlayer bonding in L-PBF. Source [25]

1.3.5 Scan Strategy

The scan strategy directs the laser's exposure of each layer, such as whether it should be unidirectional, island-based, or alternating hatch orientations. It has a significant effect on how heat spreads, how much residual stress remains, how things bend, and how the microstructure is oriented. By switching or rotating scan vectors across layers, you can help prevent heat buildup and reduce anisotropy. Choosing the proper scan approach improves the machine's performance and keeps its size stable.

1.4 Volumetric Energy Density

Volumetric Energy Density (VED), also known as Bulk Energy Density (BED), is a measure of the amount of laser energy delivered to a unit volume of powder during L-PBF. The L-PBF process involves simultaneous interactions among multiple parameters, including laser power, scanning speed, hatch spacing, and layer thickness [26]. This means that you can't figure out how much energy is going to the powder bed from just one of these parameters. VED gives a single number that represents the effective energy input required to melt, consolidate, and bond the powder particles in each layer. This is why it is one of the most common ways to estimate component density, how the melt pool will behave, how defects will form, and how the microstructure will change [27].

The standard mathematical expression for VED is:

$$\mathrm{VED} = \frac{P}{v \cdot h \cdot t} \tag{1.1}$$

Where:

- P = Laser Power (W)
- v = Scanning Speed (mm/s)
- h = Hatch Spacing (mm)
- t = Layer Thickness (mm)

The VED number indicates the amount of energy delivered per cubic millimetre of treated material, considering these four factors. This metric lets you compare different parameter combinations on a single scale, which might help you estimate how the print will turn out. Low VED values are often associated with poor melting, large holes, weak bonding, and rough surfaces. On the other hand, very high VED values can cause the melt pool to become unstable, leading to balling, keyhole porosity, or compositional vaporization. The best VED values depend on the material type, the powder properties, and the desired microstructure. However, they usually fall within a narrow range that ensures complete melting without causing overheating [28].

So, VED/BED is an essential part of studies aimed at optimizing L-PBF parameters. This is especially true when used with machine-learning-based frameworks such as artificial neural networks.

1.5 Motivation

L-PBF has become a handy way to make things; however, achieving consistent print quality still depends heavily on selecting the proper process parameters. Changes in laser power, scanning speed, hatch spacing, and layer thickness significantly affect how the melt pool behaves, how defects form, how porosity is distributed, and how well the material performs. As industrial uses move toward higher standards of dependability, dimensional accuracy, and material performance, there is a growing need for automated, data-driven optimization processes that reduce the need for human parameter selection [29]. Conventional optimization techniques in L-PBF predominantly rely on empirical principles, trial-and-error methods, or streamlined analytical models. These methods have difficulty showing the nonlinear, multi-parameter interactions that control the formation of defects, such as lack-of-fusion pores, keyhole porosity, and local thermal instability. So, traditional methods often require extensive testing and still don't yield reliable, generalizable forecasts for novel parameter combinations. This constraint underscores the need for predictive models that can elucidate deeper interdependencies within the process [30].

Machine learning (ML) techniques offer a viable avenue for interpreting intricate, multidimensional data and improving the prediction of microstructural flaws, density variations, and melt-pool stability. Previous studies have shown that ML-based regression models can effectively forecast defect content and support the development of process maps in L-PBF [31]. Building on this foundation, the present study proposes a novel expansion by including artificial neural network (ANN) error quantification into the recalculation of volumetric energy density (VED/BED). Using the ANN's mean-squared error, an updated energy descriptor is generated and compared with values reported in the literature. This provides us with new insights into the sensitivity of energy-based metrics used for L-PBF optimization. This progress supports the larger goal of developing innovative, automated, and data-driven frameworks to optimize parameters in metal additive manufacturing [32].

1.6 Problem Description

L-PBF is one of the most advanced technologies for making metal parts; however, achieving consistent part quality remains a significant challenge. The process involves melting and solidifying quickly, and many factors, such as laser power, scanning speed, hatch spacing, and layer thickness, affect the rate of melting and solidification. All these factors work together to affect the melt-pool geometry, thermal gradients, consolidation quality, and, ultimately, the density and number of defects in the finished part. Because these interactions are so complex, even small changes in parameter combinations can result in significant shifts in porosity, surface morphology, microstructure, and mechanical performance. To make sure that processes stay stable, you need to know not just the individual parameters but also how they interact with each other in a nonlinear way. Conventional optimization approaches in L-PBF often struggle to capture the complex interactions among process parameters and melt-pool behaviour. In addition, trial-and-error experimentation is costly in terms of material consumption, machine time, and effort. Machine learning offers a promising alternative for modelling nonlinear relationships, although its reliability depends on model structure, feature selection, and data quality. Therefore, this study uses artificial neural networks and literature-derived datasets to evaluate L-PBF parameter effects and improve VED/BED assessment through prediction-error-based analysis [28].

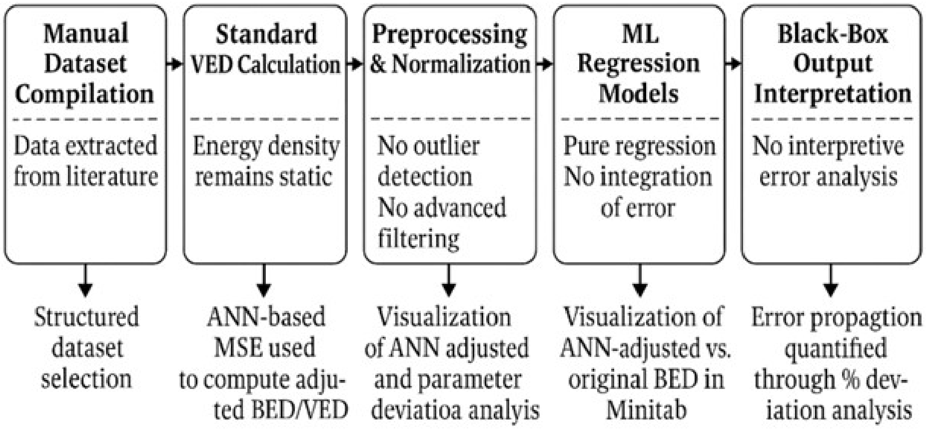

FIGURE 1.9: The block diagram illustrates the scope of this thesis, highlighting key limitations in conventional L-PBF optimization, the proposed ANN-based solutions, and the techniques employed

1.7 Objectives

The aim of this thesis is to develop and evaluate an artificial-neural-network-based framework for analysing the influence of key L-PBF process parameters on NiTi part quality, and to examine how ANN prediction error can be incorporated into the VED/BED formulation for improved process interpretation. The study's particular goals are as follows:

i. To compile and preprocess a validated literature-based dataset of selected L-PBF process parameters and corresponding output values for NiTi.
Expected outcome: a structured dataset suitable for model development and analysis.

ii. To develop ANN models in MATLAB using the selected L-PBF process parameters as inputs and the chosen quality metric as the output.
Expected outcome: trained ANN models capable of predicting the output response.

iii. To evaluate the performance of the developed ANN models using quantitative measures such as mean squared error (MSE) and correlation coefficient (R), and to identify the best-performing model.

Expected outcome: a clear comparison of model accuracy and selection of the most reliable ANN model.

iv. To recalculate VED/BED values by incorporating ANN prediction error into the conventional energy density formulation.

Expected outcome: a set of ANN-adjusted VED/BED values for comparison with the original values.

v. To compare the original and ANN-adjusted VED/BED values using percentage deviation and statistical analysis in MATLAB, Excel, and Minitab.

Expected outcome: quantified differences showing the effect of prediction error on energy-density interpretation.

vi. To determine whether ANN-adjusted VED/BED provides a more informative basis for analysing L-PBF parameter sensitivity than the conventional formulation.

Expected outcome: an evidence-based conclusion on the usefulness of the adjusted energy-density approach.

1.8 Scope of Thesis

This thesis aims to define the study's boundaries and clarify the methodological and analytical contributions that have improved parameter optimization in Fusion L-PBF. This work encompasses the following principal areas:

1.8.1 Use of Previously Published Laser Powder Bed Fusion Parameter Data

This thesis uses process parameter combinations extracted from the published work of Obeidi (2022), including laser power, scanning speed, and pulse frequency. These experimentally reported variables, together with the corresponding relative-density values for 40 μm and 80 μm layer-thickness conditions, form the dataset used for ANN modelling in the present study.

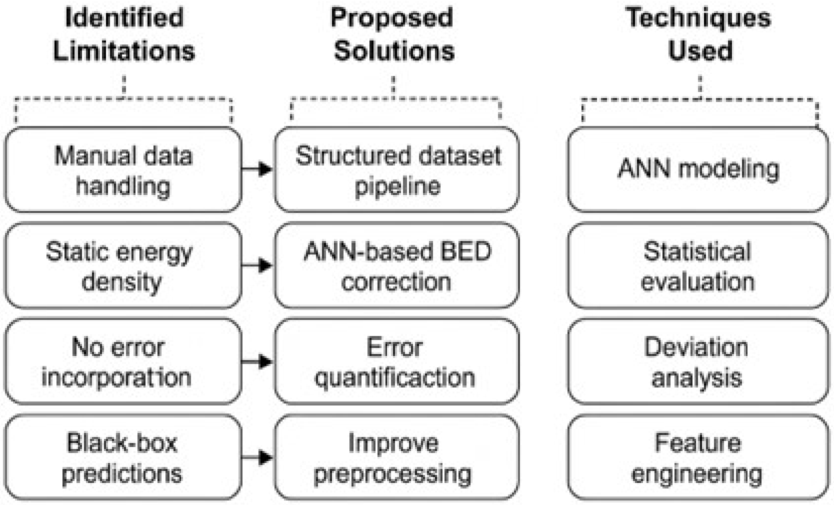

FIGURE 1.10: The block diagram illustrates the scope of this thesis, highlighting key limitations in conventional L-PBF optimization, the proposed ANN-based solutions, and the techniques employed

1.8.2 Development of an ANN-Based Predictive Framework

The research focuses on developing an artificial neural network (ANN) model capable of learning nonlinear correlations between L-PBF parameters and designated output variables. The ANN is the primary tool for making predictions. It uses the input parameter set to make guesses about print quality metrics.

1.8.3 Error Quantification Through Mean Squared Error

The mean squared error metric is used to assess how well the model performs. This is an essential aspect of the procedure, as it is subsequently used to recalculate the volumetric energy density (VED/BED). This step adds an interpretive layer that isn't there in standard L-PBF optimization methods.

1.8.4 Re-Estimation of Energy Density Using ANN Error

The thesis incorporates the recalculation of VED/BED by integrating ANN-derived error data into the conventional energy density equation. This improvement provides a new perspective on energy-based optimization frameworks by showing how inaccurate predictions affect physical process characteristics.

1.8.5 Statistical and Comparative Analysis Across Multiple Software Tools

The thesis uses MATLAB, Excel, and Minitab to analyze and present results. Outputs include BED deviation, % error comparisons, and graphical performance evaluations, facilitating a thorough examination of parameter behavior and model resilience.

1.8.6 Interpretation Within the Context of Laser Powder Bed Fusion Process Optimization

The scope includes an interpretive assessment of how ANN-adjusted energy density values may influence future parameter selection strategies. This interpretation remains grounded within the operational constraints of L-PBF and focuses on supporting data-driven optimization rather than proposing machine-level control strategies.

1.9 Thesis Overview

This thesis has six chapters, each of which discusses an essential component of the machine-learning-assisted optimization framework for the L-PBF process.

Chapter 1: Introduction, Problem Statement, and Findings talks about the basics of L-PBF, its most important parameters, and why machine learning techniques are being used. It then describes the problem, the study's goals, and its scope.

Chapter 2: Literature Survey This Chapter provides a comprehensive analysis of the latest developments in additive manufacturing and machine learning, focusing on past attempts to optimize parameters and pinpointing research needs pertinent to LPBF systems.

Chapter 3: Materials and Methods This chapter describes the resources, datasets, and methods utilized in this work. This includes obtaining process parameters from literature, defining input and output variables, and determining the volumetric energy density. It explains how to build an artificial neural network (ANN) model in MATLAB. It discusses the network's structure, training procedures, how to check for errors, and how to incorporate ANN-derived MSE into recalculated BED/VED measurements.

Chapter 4: Results and Discussions It shows the results of analyses done with MATLAB, Excel, and Minitab. These results include how well the ANN predicted values, how the energy density values were changed, how percentage deviation comparisons were made, and how the results were shown in graphs. This chapter also discusses what ANN-refined energy measures mean for improving the L-PBF process.

Chapter 5: Conclusions and Future Work It summarizes the study's key findings, discusses its limitations, and suggests ways future research could improve data-driven optimization and intelligent control strategies for L-PBF systems.

Chapter 2

Literature Review

2.1 Overview of Metal Additive Manufacturing

Additive Manufacturing (AM) has become a revolutionary type of technology that makes it possible to create three-dimensional parts by putting together layers of material. AM manufactures parts directly from digital CAD models, which gives designers more freedom and makes better use of materials than traditional subtractive and formative manufacturing methods that cut or reshape bulk material [33]. Many researchers agree that AM is a vital factor in the future of manufacturing, especially for applications that need complicated shapes, lightweight structures, internal channels, or bespoke functionality [34]. There are many types of processes in the metal AM field, such as Directed Energy Deposition (DED), Binder Jetting, and Powder Bed Fusion (PBF). Each one is best for a distinct type of industry. PBF technologies are the best of these because they can achieve high-dimensional accuracy, acceptable feature resolution, and microstructural control.

L-PBF is one of the most studied and used metal AM methods in industry. It is part of the larger PBF family. It entails distributing a tiny layer of metal powder onto a build platform and selectively melting the powder using a high-energy laser that follows the part's sliced shape. To make a fully dense part, layers are fused. Research indicates that L-PBF provides enhanced precision relative to DED and other fusion-based methods, attributable to its minimal melt pool size, uniform powder distribution, and regulated heat gradients [35, 36]. Because of this, L-PBF is being used in the aerospace, biomedical, automotive, and energy industries to make lightweight structural parts, implants, heat exchangers, and turbine parts.

Researchers regularly note that L-PBF is highly sensitive to its process parameters, including laser power, scanning speed, hatch spacing, and layer thickness. These factors all work together to affect the stability of the melt pool, the creation of porosity, the evolution of the microstructure, and the mechanical performance [37]. Even little mistakes in choosing parameters might cause problems like lack-of-fusion porosity, keyhole pores, balling phenomena, and thermal distortions. Moreover, numerous writers underscore that the nonlinear and interdependent characteristics of these parameters render predictive modelling difficult when exclusively utilizing empirical or analytical formulations [38].

As a result, the increasing complexity of L-PBF and its sensitivity to parameter interactions have led to the incorporation of advanced data-driven models, such as machine learning and artificial neural networks, to enhance prediction accuracy, optimize process parameters, and diminish dependence on expensive trial-based experimentation. This constitutes the scientific basis for the modelling method employed in the current thesis.

2.2 Research on Laser Powder Bed Fusion in Literature

A significant amount of research has investigated the correlations between L-PBF process parameters and part quality, yielding a range of experimental, imaging, and data-driven studies. Initial experimental studies conducted by King et al. and DebRoy et al. delineated melt-pool regimes and correlated energy input with defect types, including keyholing and lack of fusion, thereby affirming the significance of energy measures in process management [36, 39]. These foundational publications continue to be extensively referenced as they correlate physical events with process windows. Tapia and Elwany created spatial Gaussian-process models to predict porosity. These models indicate that advanced statistical methods can figure out where pores are likely to occur across different structures. Later research used high-resolution X-ray and synchrotron imaging to follow pore nucleation and keyhole dynamics in alloys like Inconel 718 and Ti6Al4V. These imaging investigations provide ground-truth labels for pores and melt-pool geometries, which are used to train modern machine learning models [40].

Recent data-driven studies have advanced process optimization. Minkowitz et al. employed ExtraTrees regression for the optimization of the AlSi10Mg process, showcasing competitive predictive efficacy for relative density through tree-based ensembles [41]. Wang et al. [36] introduced a material-agnostic machine learning methodology that facilitates high relative density across various alloys, demonstrating the viability of generalizable machine learning pipelines for process mapping. Concentrated investigations on NiTi and analogous functional alloys indicate supplementary, alloy-specific difficulties. Liu et al. and Choudhary et al. investigated the influence of hatch spacing and laser power on NiTi density and functional response. They discovered that reduced hatch spacing and optimized power windows enhance density and shape-memory behaviour, although they may intensify Ni evaporation or compositional shifts under excessive thermal input. Multiple publications have indicated that build orientation and powder characteristics influence oxygen uptake and phase formation, hence hindering the straightforward transfer of parameter windows across machines or powders [42, 43].

Various formulations of a problem yield distinct machine learning solutions. The tesi.pdf survey examined various machine learning algorithms (BR, DTR, GBR, GPR, KNN, RFR, SVR). It concluded that with appropriate hyperparameter tuning (such as SVR with an RBF kernel), density forecasts can achieve high accuracy, with optimized parameter sets yielding over 99% relative density in certain instances. However, this study typically offers only forecasts and static process maps, failing to utilize prediction uncertainty to modify physical descriptions. In-situ monitoring and sensor fusion approaches, including thermal imaging, acoustic emission, and photodiodes, have been employed to detect porosity and single-track faults, providing real-time data for machine learning models [44].

Gorganneja et al. have shown notable success in porosity identification and keyhole prediction when imaging data is available. Nonetheless, these methodologies require intricate instruments and extensive labelled datasets. Identified issues across various studies include: (i) nickel evaporation in NiTi, altering composition and transformation temperatures; (ii) microstructural heterogeneity resulting from local thermal gradients; and (iii) residual porosity and lack-of-fusion defects arising from insufficient energy input or incorrect hatch spacing. XCT, Archimedes tests, and metallography have consistently demonstrated these phenomena [45].

Despite these enhancements, there remain several deficiencies. Many optimization studies regard VED/BED as static and neglect to incorporate model prediction error in the revaluation of energy descriptors; only a few investigations create a closed-loop system that employs ML residuals to adjust physical process parameters. The scope and variety of the dataset pose challenges for generalizability, making its implications difficult to comprehend. Machine learning algorithms generate accurate predictions; yet, they frequently fail to translate these predictions into actionable alterations in physical parameters. This specific deficiency necessitates the ANN-based, error-integrated VED re-estimation methodology established in this study.

2.3 Machine Learning and ANN Applications in Metal AM

2.3.1 Overview: Machine-Learning Methods Used in AM

Current advances in metal AM technology also see a growing use of machine-learning techniques in combination with in-situ monitoring for process instability detection and quality prediction in a real-time fashion. Figure 2.1 illustrates a typical machine-learning process chain including optical sensing and image analysis using convolutional neural networks (CNNs) for anomaly detection in L-PBF processes. Machine learning techniques used in additive manufacturing include conventional regression and ensemble methods (such as linear regression, SVR, Random Forest, and Gradient Boosting), kernel methods, and newer neural-network methods (like convolutional, recurrent, and dense feed-forward networks) [46]. Reviews reveal two concurrent study avenues: (a) process monitoring and defect identification using imaging and signal characteristics; and (b) process parameter-property correlation employing tabulated experimental or simulated datasets. Survey articles highlight that CNNs and hybrid vision + ML pipelines are widely used for detection tasks, while ensemble regressors and ANNs are often used for property prediction and optimization, since they can easily map nonlinear relationships [47].

2.3.2 ANN as a Nonlinear Predictive Model

Artificial neural networks (ANNs) are composed of interconnected layers of neurons, which make it possible to model complex nonlinear relationships among input processing variables and corresponding output responses. The typical feed-forward ANN configuration used in regression problems in Additive Manufacturing is shown in Figure 2.1. Artificial neural networks (ANNs) are frequently used because they can approximate complex, non-linear processes without using physical models. Behnam Ahmadikia exhibited an ANN framework for PBF parameter optimization, emphasizing its capacity to forecast target qualities from various input parameters and facilitate search over multi-dimensional parameter spaces. Maleki et al. also used a neural network model on Ti-6Al-4V to link process variables to tensile parameters. This model was more accurate than simple regressions when there were enough features. These investigations demonstrate that appropriately built ANNs can encapsulate interactions among laser power, scan speed, and hatch spacing that linear methods inadequately express [48, 49].

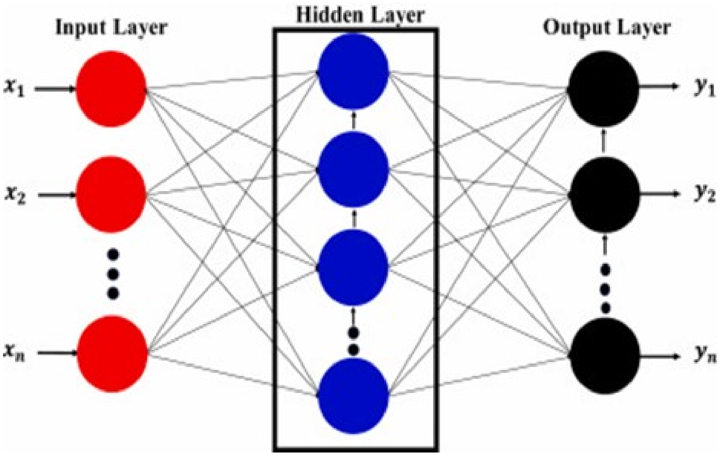

Figure 2.1: Typical feedforward artificial neural network (ANN) architecture for regression, consisting of an input layer (process parameters), one or more hidden layers with weighted connections and nonlinear activation functions, and an output layer representing [50]

2.3.3 Studies Predicting Density, Porosity and Melt-Pool Geometry

Numerous studies have employed machine learning to forecast relative density and porosity based on process inputs or in-situ sensor characteristics. Okaro et al. utilized semi-supervised learning for fault identification in L-PBF constructions, demonstrating efficient anomaly detection with a small number of labels. Zhang et al. utilized thermal imaging to extract melt-pool and plume features for defect prediction by machine learning, whereas Ren et al. integrated high-speed X-ray datasets with machine learning to forecast pore evolution and monitor melt-pool regimes. These studies show that these methods work well on small datasets, and many of them report high classification or regression scores when imaging or high-fidelity experimental labels are used [51, 52].

This type of ANN architecture, as shown in Figure 2.2, is widely employed in L-PBF research to capture the nonlinear relationships between process parameters and multiple quality metrics. The hidden layers enable the network to model complex interactions that cannot be described using linear or empirical formulations. Such multi-output ANN structures allow simultaneous prediction of density, surface quality, and mechanical properties from a common parameter set.

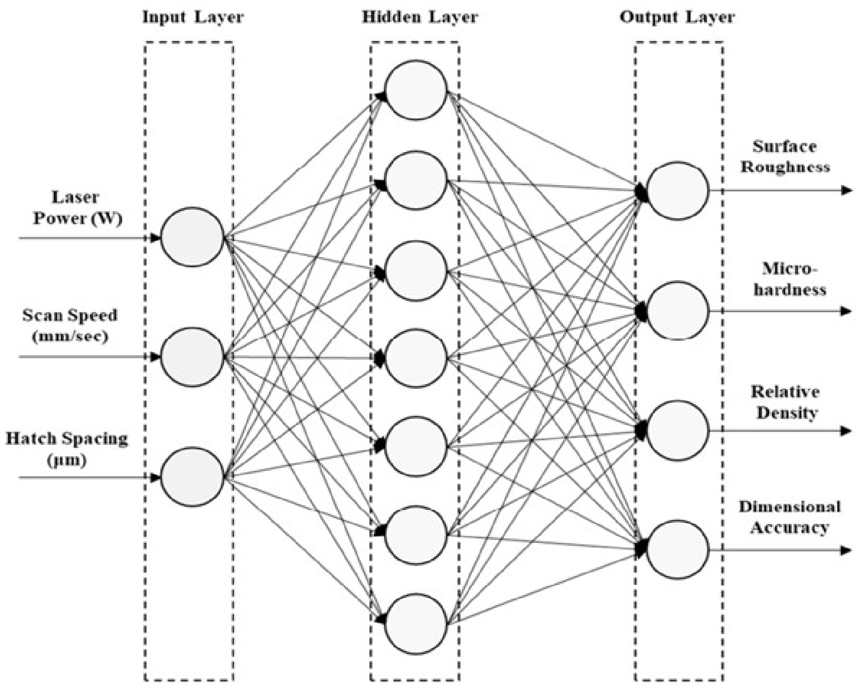

Figure 2.2: Schematic representation of an artificial neural network (ANN) used for predicting multiple L-PBF output properties from process parameters. The input layer consists of laser power, scanning speed, and hatch spacing, which are processed through one or more hidden layers with weighted connections and nonlinear activation functions to predict output responses such as relative density, surface roughness, microhardness, and dimensional accuracy [53]

2.3.4 Reported Shortcomings of ANN Approaches

Authors frequently identify several practical constraints of ANN-based models in AM: (i) the failure to incorporate prediction error into physical parameters models generate predictions but seldom adjust derived process descriptors (e.g., VED/BED) based on residuals; (ii) the absence of closed-loop feedback, few studies utilize model uncertainty to enhance process maps or experimental plans adaptively; (iii) limited datasets and transferability datasets are often small, machine-specific, or alloy-specific, which diminishes generalizability; and (iv) a lack of interpretability ANN outputs can sometimes be opaque, hindering the translation into actionable process modifications. Recent reviews and domain studies have regularly pointed out these problems [54].

Because L-PBF parameters are not linearly related and we need to connect prediction uncertainty to a physics-based descriptor (VED/BED), ANNs are a good choice. They can learn multi-input/multi-output mappings, be tuned for small datasets (with regularization, dropout, or cross-validation), and give residuals (like MSE) that are easy to get and use again. This thesis expands upon previous implementations of artificial neural networks (ANNs) by utilizing an ANN not only for prediction but also to measure error and integrate that error into the energy-density calculation, thus filling a recognized gap in the existing research [55].

Although Gaussian-process and response-surface approaches may be well suited to small datasets, ANN models were retained in the present work because the primary aim of the thesis was not broad algorithm benchmarking, but the development of an ANN-based framework in which prediction error could be incorporated into the recalculation of VED/BED. Therefore, ANN was used as the central predictive model for the proposed error-adjusted energy-density analysis, while alternative regressors are recommended for future comparative investigation.

2.4 Identified Research Gaps and Study Motivation

Existing machine-learning studies in additive manufacturing mainly follow two directions: process monitoring and defect detection using image or sensor data, and process parameter–property prediction using tabulated experimental or simulated datasets. In L-PBF research, models such as ANN, SVR, Random Forest, and other regression approaches have been used to predict outcomes such as density, porosity, and defect formation. However, most of these studies primarily report prediction performance using metrics such as R^2, MSE, or RMSE, while giving limited attention to how model error influences the interpretation of derived process descriptors such as volumetric energy density (VED/BED) [56, 57]. A clear gap in the literature is the lack of studies that use prediction error not only as an accurate measure, but also as a means of reassessing energy-based process interpretation. Although VED/BED is widely used to describe L-PBF processing conditions, few studies investigate how deviations between predicted and reference results may affect the reliability or sensitivity of such descriptors [58, 59].As a result, there remains limited understanding of how model uncertainty can be linked to the interpretation of parameter windows and process behaviour.

Another limitation is that many reported ML frameworks function mainly as black-box predictors, with limited interpretive analysis beyond model accuracy. While existing studies often focus on predicting density or porosity, the use of ANN-derived prediction error to recalculate or reinterpret physically defined process descriptors remains rarely explored in the current literature [60]. This creates an opportunity to develop a framework that not only predicts L-PBF outcomes but also examines how model error affects the evaluation of energy-density-based parameters.

TABLE 2.1: Summary of Identified Gaps and Contributions of This Study [56–58]

Identified Gap in Literature	**Contribution of This Thesis**
VED/BED is always treated as static	ANN-derived error used to recompute VED/BED
No % deviation analysis	% deviation between the original and the ANN-adjusted BED evaluated
Single-tool analysis common	MATLAB + Excel + Minitab combined for multi-tool validation
No ANN-driven recalculation of energy metrics	ANN error integrated directly into energy-density formulation
Lack of interpretive frameworks	Error mapped to physical meaning and parameter sensitivity

Chapter 3

Materials and Methods

This chapter provides insight into the methodological approach adopted to analyze and develop the L-PBF Fusion process parameters via artificial neural networks and the recalculation of Energy Density. The steps outlined in the proposed workflow in the chapter combine the processing of dataset selection from the existing literature [61], ANN model building, prediction error analysis, and the subsequent application of the prediction error in the calculation of volumetric energy density. The method adopted in the chapter has been specifically designed to feed into the research gaps identified in Chapter 2 of the thesis.

The chapter structure follows the overall reasoning pattern shown in the reference thesis supplied by the supervising professor, extended by another analysis step in the context of errors. MATLAB serves the development of the ANN model, Excel helps to carry out a numerical re-calculation of adjusted energy values to calculate the predicted efficiency more accurately, while Minitab analysis helps in deviation analysis. Taken together, all these steps form a complete workflow process to relate the accuracy of prediction to the physical processes of the L-PBF system.

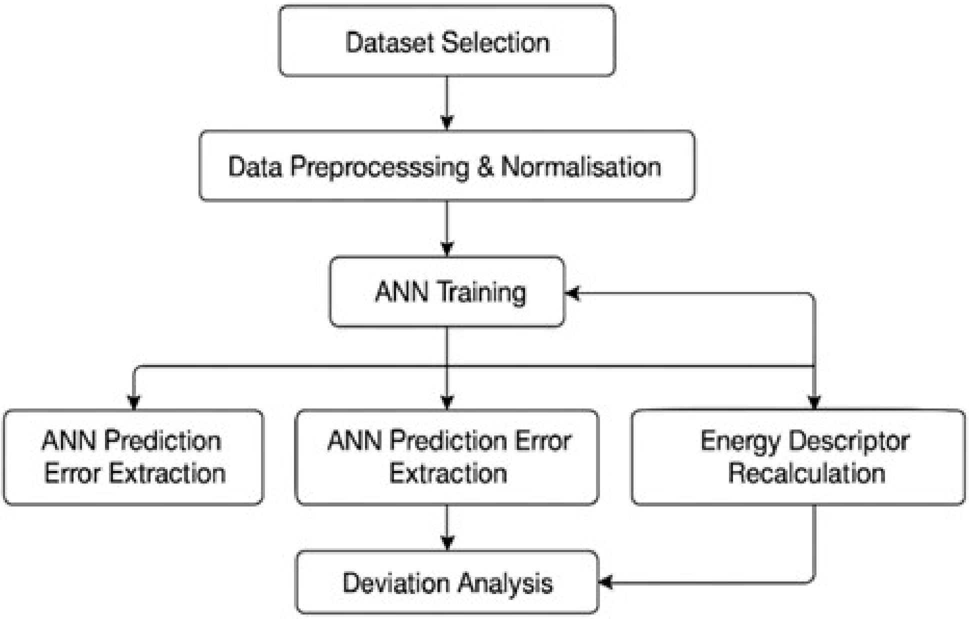

FIGURE 3.1: Methodological workflow summarizing the complete analysis pipeline, including dataset selection, preprocessing, ANN model training, prediction error extraction, energy descriptor recalculation, and deviation analysis

3.1 Dataset Selection and Parameter Extraction

The dataset used in this study was extracted from the published work of Obeidi (2022). For transparency and reproducibility, the full set of input parameter combinations and corresponding measured relative-density values used for ANN modelling is presented in Appendix A. The source study reported 27 design-of-experiment parameter combinations based on three input variables: laser power (140, 160, 180 W), scanning speed (400, 550, 700 mm/s), and pulse frequency (2, 6, 10 kHz). For each parameter combination, experimentally measured relative-density values were reported for two layer-thickness conditions, 40 µm and 80 µm, which were used in the present work as the target outputs for ANN modelling. Additional process settings in the source study, such as hatch spacing, hatch rotation angle, and duty cycle, were kept fixed and were therefore not treated as variable inputs in the present dataset.

The extracted data were organized in spreadsheet form so that each row represented one complete parameter combination together with its corresponding relative-density outputs. This structure provided a consistent input–output mapping for ANN regression modelling. Since the present thesis is based on a single published NiTi dataset rather than a merged multi-study dataset, no cross-study harmonization of different experimental protocols was required. Instead, the data were checked for completeness, internal consistency, and compatibility with the modelling workflow before being used for ANN training and subsequent VED/BED recalculation.

3.2 Experimental Context from Literature

In the present thesis, no new experimental design, such as CCD or Box–Behnken Design, was conducted by the author. The response-surface analysis was performed in Minitab by fitting regression surfaces to the literature-derived dataset extracted from Obeidi (2022). Therefore, the statistical surfaces reported in this work are based on post hoc modelling of published data rather than on a newly designed experimental campaign. There appears to be a general trend of utilizing the NiTi powders in a prealloyed form having a composition close to equiatomic with a particle size ranging between 15-45 µm. The powder analysis in the experiments may include scrutiny of the particle size distribution, morphological analysis in some cases, and chemical analysis performed by techniques like inductively coupled plasma optical emission spectroscopy or EDS analysis.

Experimental results used in the L-PBF process-property modeling simulation range from studies utilizing commercial powder bed fusion systems having the capability of varying the output powers of lasers (roughly estimated to range between 50-400 Watts) to speeds of up to 2000mm per second. Some of the post-processing experiments conducted in the simulation involve optical microscopy analysis, scanning electron microscopy analysis (SEM analysis), X-ray diffractions (XRD analysis), differential analysis of calometric scans (DSC analysis), micro-hardness tests, or Archimedes' principles for measuring density. These experiments produce output values of density or mass per centimeter. There also exist some studies that utilize structured Design of Experiments (DoE) designs, more specifically, the fractional factorials or central composite designs, to vary the L-PBF parameters in a controlled manner. The boundaries of the L-PBF parameters range from a laser power of 100-300W to a speed of 200- 1200 mm/s. Additionally, the hatch spacing ranges between 50-200 μm. Finally, the thickness may vary between 20-100 μm. These designs allow the creation of a dataset of 20-50 sets of parameters.

3.3 Data Preprocessing and Normalization

Each layer-thickness condition was analyzed as a separate 27-sample dataset. For ANN training, the data were randomly divided into 70% training, 15% validation, and 15% testing subsets, corresponding to 19, 4, and 4 samples, respectively. Before model development, the extracted dataset was checked for completeness, consistency, and suitability for ANN regression. Since the present work used a single literature-derived dataset from Obeidi (2022), preprocessing was mainly concerned with arranging the data in a consistent numerical format for MATLAB rather than harmonizing multiple sources with different reporting conventions.

The selected input variables were laser power, scanning speed, and pulse frequency, while relative density was used as the target output for each layer-thickness condition. The data were organised into a structured input–output format so that each row represented one experimental parameter combination and its corresponding measured response. Principal Component Analysis (PCA) was not applied because the dataset contained only three physically meaningful input variables, and dimensionality reduction would reduce interpretability without offering a clear advantage for such a low-dimensional parameter set. If repeated runs are carried out without a fixed random seed in MATLAB, small differences may occur due to stochastic data partitioning and network-weight initialization.

3.4 ANN Architecture and Model Training

Artificial Neural Network (ANN) regression models were developed in MATLAB using the Neural Network Fitting tool to capture the nonlinear relationship between selected L-PBF process parameters and relative density. In the present study, the input variables were laser power (P), scanning speed (v), and pulse frequency (f), while the target output was the experimentally reported relative density for the corresponding layer-thickness condition.

Separate ANN models were developed for the 40 μm and 80 μm datasets, each consisting of 27 observations with three input features and one continuous output response. A feed-forward neural network architecture was adopted for the regression task. Based on the implemented MATLAB setup, the network used a single hidden layer with 10 neurons. This architecture was selected to provide sufficient nonlinear mapping capability while remaining suitable for the relatively small dataset used in the present work. The ANN models were trained and evaluated independently for each layer-thickness condition.

Three ANN training algorithms were considered in this study: Levenberg Marquardt, Bayesian Regularization, and Scaled Conjugate Gradient, implemented in MATLAB using the training functions `trainlm`, `trainbr`, and `trainscg`, respectively. The performance criterion used during training was mean squared error (MSE). For all models, the dataset division followed a 70%/15%/15% ratio for training, validation, and testing, corresponding to 19, 4, and 4 observations, respectively. MATLAB used random data division to assign samples to these subsets.

The Levenberg–Marquardt algorithm was selected because of its fast convergence and established suitability for small- to medium-sized nonlinear regression problems. The Levenberg–Marquardt algorithm updates weights using a Jacobian-based approximation computed internally by MATLAB during training; however, the explicit Jacobian matrix was not extracted and reported separately in this study. For LM and SCG, model training proceeded until the stopping criterion was reached, with the MATLAB output indicating convergence based on the minimum gradient condition. In contrast, Bayesian Regularization controlled overfitting through its internal regularization mechanism rather than relying on conventional validation-based early stopping.

Since the models were trained using MATLAB's Neural Network Fitting environment, data partitioning, training, and regression evaluation were handled within the same workflow. The same input variables and dataset structure were used across all three training algorithms to ensure a fair basis for comparison. However, unless a fixed random seed is explicitly imposed in MATLAB, repeated runs may produce slightly different data partitions and initialization states.

After training, each ANN produced predicted relative-density values together with associated MSE and regression correlation values. These outputs were then used in the subsequent stages of the study for comparative model assessment and for the recalculation of ANN-adjusted VED/BED values.

3.5 Model Performance Evaluation Using Mean Squared Error

The present study uses Mean Squared Error (MSE) as the primary performance metric because the ANN models were developed for continuous-output regression, with relative density as the target variable. MSE is particularly suitable in this context because it measures the average squared prediction error and penalizes larger deviations more strongly, thereby providing a sensitive indication of model accuracy. This is important in the current work because the ANN prediction error is later incorporated into the adjusted VED/BED analysis. Metrics such as precision, recall, and F1-score were not used because they are designed for classification tasks involving discrete categories, whereas the present study predicts continuous numerical values rather than class labels:

$$\mathrm{MSE} = \frac{1}{n}\sum_{i=1}^{n}(y_i - \hat{y}_i)^2 \tag{3.1}$$

where y_i denotes the experimental output value obtained from the literature and $\hat{y}_i$ represents the corresponding ANN-predicted value.

In addition to MSE, the regression correlation coefficient (R) was used to evaluate the strength of agreement between ANN-predicted and experimental values. In MATLAB regression plots, R represents the linear correlation between the predicted outputs and the target outputs, with values closer to 1 indicating stronger agreement and values closer to 0 indicating weak correlation. Because the ANN performance in this study is reported in the results chapter using R-values for the training, validation, and test subsets, the regression coefficient R was adopted as the secondary performance indicator alongside MSE.

During model development in MATLAB, these performance measures were monitored over the training, validation, and test subsets to assess prediction accuracy and generalization capability. For LM and SCG training, early stopping based on validation performance was used to reduce overfitting, while Bayesian Regularization controlled overfitting through its internal regularization mechanism.

In the present study, MSE was not used only as a performance indicator, but was also incorporated into the recalculation of VED/BED to examine how prediction uncertainty affects the interpretation of energy-based process descriptors.

3.6 Energy Density Volumetric Energy Density and Bulk Energy Density Recalculation Using ANN Error

Volumetric Energy Density (VED), also referred to in some studies as Bulk Energy Density (BED), is used to represent the nominal energy input delivered to a unit volume of powder during the L-PBF process. In its conventional form, VED is calculated as:

$$\text{VED} = \frac{P}{v \cdot h \cdot t} \tag{3.2}$$

where P is the laser power, v is the scanning speed, h is the hatch spacing, and t is the layer thickness. This expression provides a theoretical energy-input descriptor based on process parameters under idealised conditions.

In the present study, however, the purpose was not only to calculate the nominal VED, but also to examine how ANN prediction uncertainty influences the interpretation of that energy descriptor. For this reason, an adjusted energy term, denoted as VED*, was introduced by incorporating the ANN prediction error, represented by Mean Squared Error (MSE), into the recalculation framework. The adjusted descriptor was used as a comparative quantity rather than as a replacement for the conventional VED equation.

In practical terms, the conventional VED was first calculated from the experimental parameter set reported in the literature. A second value, referred to as ANN-adjusted VED, was then obtained by applying the ANN-derived error term within the recalculation framework used in this thesis. The difference between the experimental VED and the ANN-adjusted VED was evaluated using percentage deviation:

$$\%\Delta\text{VED} = \frac{|\text{VED} - \text{VED}^*|}{\text{VED}} \times 100 \tag{3.3}$$

This percentage-deviation measure was used to assess how sensitive the energy-density interpretation was to ANN prediction uncertainty. In this way, the study extends the usual static use of VED/BED by linking predictive model error to the interpretation of energy-based process behaviour.

3.7 Software Tools Used

A multi-software approach was adopted in this research to support the development and evaluation of an ANN-based framework for analyzing L-PBF process parameters. MATLAB was the primary tool used for ANN model development, training, and extraction of performance measures such as Mean Squared Error (MSE) and regression correlation. Microsoft Excel was used for numerical recalculation of adjusted volumetric energy density values and for organizing intermediate calculations and percentage-deviation comparisons. Minitab was used to perform analysis of variance (ANOVA), Pareto analysis, and response-surface modelling for the 40 μm and 80 μm relative-density datasets. The combined use of MATLAB, Excel, and Minitab allowed prediction, recalculation, and statistical interpretation to be carried out within a consistent workflow.

Chapter 4

Results and Discussion

This chapter presents the analysis results obtained from the methodology delineated in Chapter 3, focusing on the capabilities of the established ANN framework in assessing the L-PBF parameters. These analysis results include the neurodynamic of the ANN model in terms of the optimization algorithms utilized, the quantitative analysis of the accuracy of the predictions obtained in terms of Mean Squared Error (MSE) simulation analysis, and a comparative analysis of the predicted density values from the ANN framework to the values obtained from the corresponding experimental studies for the dataset of 40 μm layers and the dataset of 80 μm layers. After the predictions achieved in the ANN framework, further analysis involves the computation of volumetric energy density values utilizing the predicted error, followed by a deviation analysis to conclude the influence of prediction uncertainty in the obtained energy values.

4.1 Dataset Summary

The source study reported 27 unique combinations of the three input parameters: laser power, scanning speed, and pulse frequency. For each parameter combination, relative density was experimentally measured at two layer-thickness conditions, 40 μm and 80 μm. Therefore, the dataset can be interpreted in two ways: as 27 unique input cases with two corresponding output values, or as 54 total observations when the two layer-thickness conditions are treated separately. In the present work, the 40 μm and 80 μm conditions were analyzed as two separate 27-sample datasets so that ANN training and performance evaluation could be carried out independently for each layer thickness.

TABLE 4.1: Summary of Dataset Characteristics

Category	**Details**
Unique input combinations	27
Layer thickness conditions	40 μm and 80 μm
Total output observations	54
Analysis approach	Two Separate 27-Sample Datasets for 40 μm and 80 μm
Laser power (W)	140, 160, 180
Scanning speed (mm/s)	400, 550, 700
Pulse frequency (kHz)	2, 6, 10
Output variable	Relative density
Derived quantities used in analysis	Computed VED, ANN-adjusted VED, MSE, % deviation
Source	Obeidi (2022) [62], pulse-wave L-PBF of NiTi alloy

4.2 ANN Training Results

This section presents the performance of the three ANN training algorithms used in this study: Levenberg–Marquardt (LM), Bayesian Regularization (BR), and Scaled Conjugate Gradient (SCG). All three algorithms were trained using the same input variables, namely laser power, scanning speed, and pulse frequency, to predict relative density for the 40 μm and 80 μm datasets. Performance is reported in terms of Mean Squared Error (MSE) and regression correlation (R), together with the corresponding train/validation/test behaviour for each model. To maintain consistency, the values reported in the text, tables, and regression discussions should refer to the same MATLAB run for each algorithm.

4.2.1 LM Algorithm

4.2.1.1 For 40 μm

In the present study, the ANN input variables were laser power (P), scanning speed (v), and pulse frequency (f). Although hatch spacing (h)It is commonly included in conventional VED formulations for L-PBF, but it was not treated as a varying input in this dataset because the source study kept it fixed. Therefore, all ANN modelling and performance analysis in this thesis were based on P, v, and $f$as the independent variables.

The Levenberg–Marquardt algorithm was first applied to the 40 μm layer-thickness dataset. Relative density was taken as the target output. The 27-sample dataset was randomly divided into training, validation, and test subsets in a 70%/15%/15% ratio, corresponding to 19, 4, and 4 samples, respectively. The LM model converged in 5 epochs, indicating stable optimization behaviour for the selected dataset. Based on the MATLAB model summary, the LM-trained ANN achieved a training MSE of 0.3357 with $R = 0.8339$, a validation MSE of 0.3194 with $R = 0.7374$, and a test MSE of 0.1344 with $R = 0.9098$. These values provide the basis for evaluating the model's predictive behaviour for the 40 μm dataset.

The regression plots for the LM model at 40 μm provide a qualitative view of the agreement between predicted and target relative-density values across the training, validation, and test subsets. In general, the points cluster around the ideal $Y = T$line, indicating that the model was able to capture the overall response trend for this dataset. However, the quantitative performance of the model should be interpreted primarily using the values reported in Table 4.2, which provides the MSE and Rvalues used in the present analysis.

Table 4.2: Training, validation, and testing performance metrics (MSE and R) for the LM-trained ANN at 40 μm layer thickness

Dataset	**MSE**	**R**
Training	0.3357	0.8339
Validation	0.3194	0.7374
Test	0.1344	0.9098

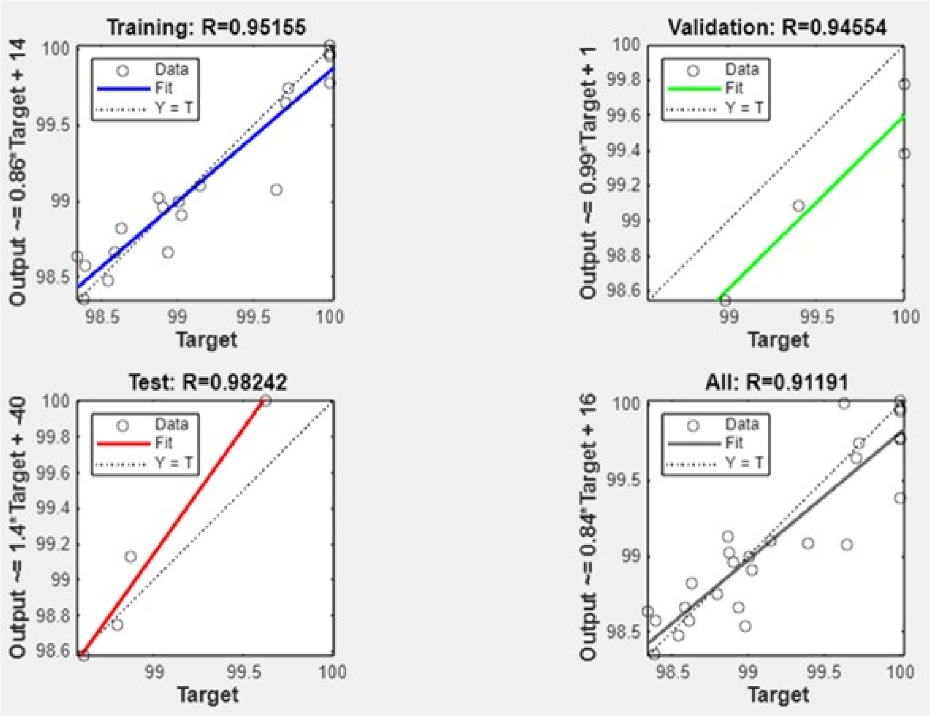

FIGURE 4.1: Regression plots for LM (40 μm) showing strong linearity and high correlation across training, validation, and test sets

4.2.1.2 For 80 μm

The Levenberg–Marquardt algorithm was also applied to the 80 μm layer-thickness dataset using the same three predictors and the same 70%/15%/15% data-division ratio. Based on the reported model summary in Table 4.3, the LM-trained ANN achieved a training MSE of 0.0011 with $R = 0.9994$, a validation MSE of 0.1492 with $R = 0.9369$, and a test MSE of 0.0730 with $R = 0.9865$. These results indicate very strong fitting and high predictive agreement for the selected data partition, although the limited dataset size means that the results should still be interpreted as exploratory.

The regression plots for the LM model at 80 μm indicate strong agreement between predicted and target values, particularly for the test subset. The visual clustering around the ideal $Y = T$ line suggests good predictive capability for the selected partition. Nevertheless, the quantitative model assessment used in this thesis should be taken from Table 4.5, which reports the numerical MSE and Rvalues adopted for comparison across ANN algorithms.

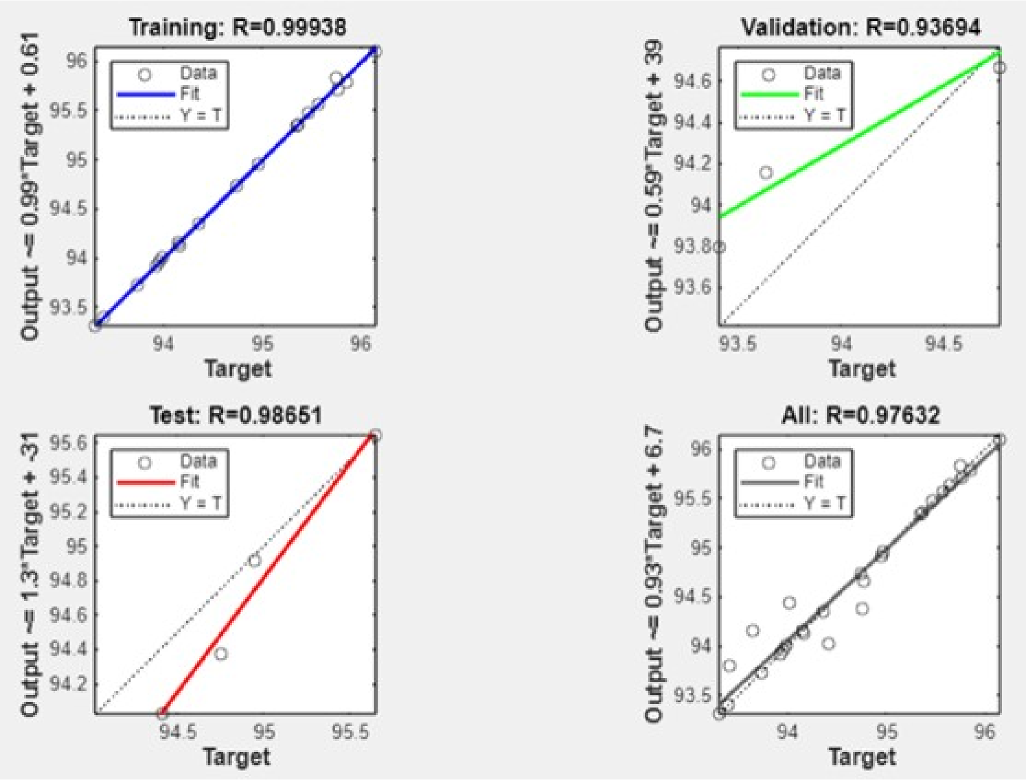

FIGURE 4.2: LM regression performance for the 80 μm dataset, illustrating excellent alignment between predicted and target values

TABLE 4.3: Performance metrics of the LM-trained ANN for the 80 μm dataset, showing MSE and R values across training, validation, and testing

Dataset	**MSE**	**R**
Training	0.0011	0.9994
Validation	0.1492	0.9369
Test	0.0730	0.9865

The regression graphs for the 80 μm dataset show the Levenberg-Marquardt (LM) model's strong predictive ability on the training, validation, and testing datasets. From the training graph with $R = 0.99938$, there is near perfection in predicting and targeting, and thus efficient learning. From the validation graph with $R = 0.93694$, though having a slightly higher deviation, there is still stability and predictability with a linear trend and thus efficient generalization for the model with varying data. From the test graph with $R = 0.98651$, there is strong predictability and fitting with precision to the actual $T = Y$ function with slight deviations, and thus efficient predictability for the model on all unknown datasets. From the overall regression analysis with $R = 0.97632$, there is efficient model behavior for all 27 datasets. From the overall graphs for the R values for the regression analysis, the LM algorithm is seen to perform well on the regression analysis for the 80 μm dataset, with higher correlations and fewer deviations, and thus efficient model behavior compared to the previous dataset for the 40 μm dataset.

4.2.2 BR Algorithm

4.2.2.1 For 40 μm

The Bayesian Regularization (BR) algorithm was applied to the 40 μm dataset. Again, the same input/output setup was utilized. Three processing factors are required for the prediction of the experimentally determined relative density. Notably enough, the main goal of the BR methodology is the avoidance of overfitting. The model was trained under a 70-15-15 categorization of data; however, BR dynamically adjusts the number of parameters instead of relying on the validation set. Convergence in the training occurred at the 217th epoch, where the maximum value of µ was reached. This was the expected occurrence for BR when the balance of regularization was obtained.

Table 4.4: Training and testing performance of the BR-trained ANN at 40 μm layer thickness. Validation values are not applicable due to BR's adaptive regularization mechanism.

Dataset	**MSE**	**R**
Training	0.0705	0.8931
Validation	–	–
Test	0.0743	0.9291

BR reduces the problem of overfitting, making the need to plot a validation curve obsolete; therefore, the MATLAB output for the validation metrics yields NaN values. Despite the challenge of overfitting, the R-value for both the train and test sets (0.8931 and 0.9291, respectively) demonstrates a strong fit.

The regression graphs for the 40 μm data under the Bayesian Regularization (BR) method show a fair and consistent predictive link between the artificial neural network (ANN) output values and the experimental densities. The training graph

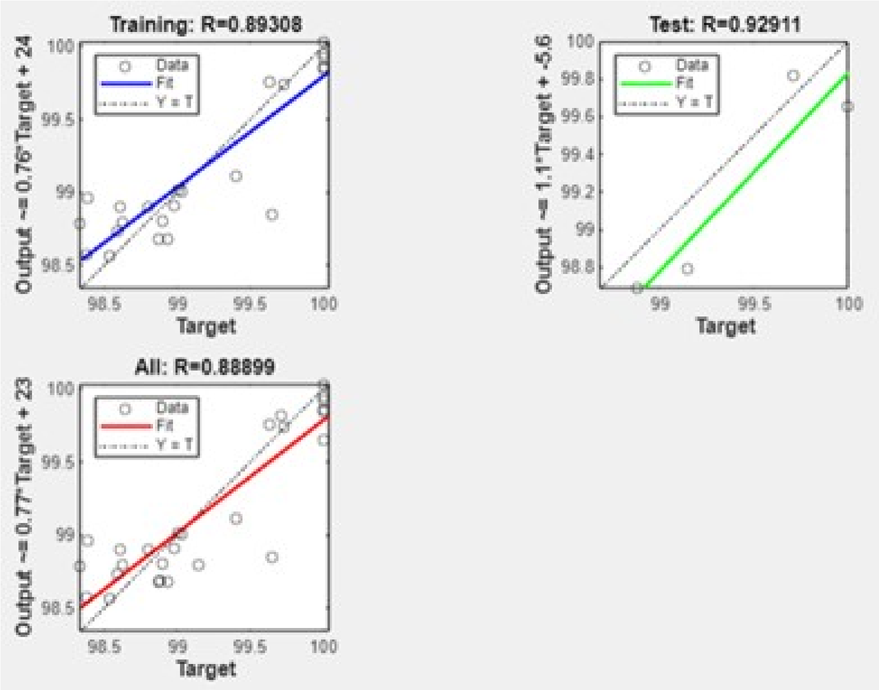

Figure 4.3: BR method regression plots (40 μm) demonstrating stable fitting behaviour with reduced sensitivity to dataset noise

(R = 0.8931) demonstrates a visible linear correlation with randomly distributed data points around the best-fit straight line, characterizing natural variability within the 40 μm measurements. The test graph demonstrates increased linear correlation (R = 0.9291) and thus successfully generalizes from the training model to more unknown datasets than within the training sample. The best-fit graph for all available data (R = 0.8889) validates consistent yet non-ideal correspondence among all 27 experimental and predicted values. The more gradual slope on both the training and all-data graphs suggests a more conservative and smooth function by regularization for preventing potential overfitting while allowing marginally reduced precision. The regression graphs for the BR method thus verify consistent predictive and resistant properties within the known noise-affected environment at the 40 μm scale.

4.2.2.2 For 80 μm

The application of the BR technique was performed for the 80 μm dataset by employing the same combination of input values and 27 measured values of relative density. In keeping with the previous application, the goal of the BR approach was to control the network weights to seek the best possible balance between fitting the data well and producing a smooth solution. The training continued until the maximum μ value was reached at 734 epochs. Indeed, the algorithm has converted to a point beyond which the complexity of the network no longer improves the output. This type of behavior tends to occur when a BR algorithm faces noisy variability in experiment results.

TABLE 4.5: Performance metrics (MSE and R) for the BR-trained ANN on the 80 μm dataset. Validation is omitted as expected with BR training

Dataset	**MSE**	**R**
Training	0.1160	0.9143
Validation	–	–
Test	0.1448	0.9337

The training R-value of 0.9143 tells how accurately the predicted output conforms to the actual production, and the test R-value of 0.9337 specifies how well the network performs on new examples. Expectedly, there would be no validation output since the Bayesian Regularization (BR) algorithm is independent of the traditional validation-stop criterion.

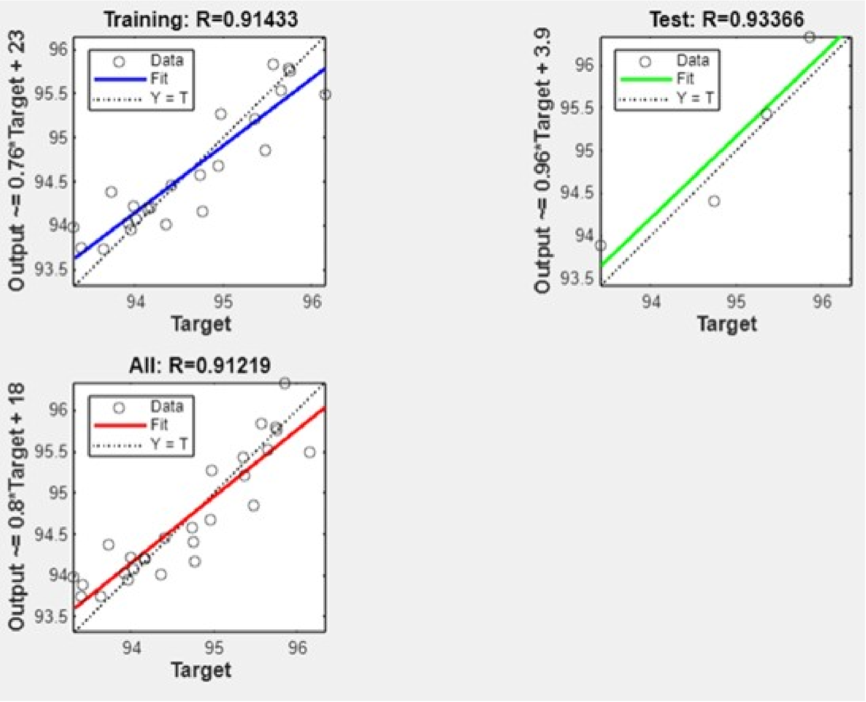

FIGURE 4.4: Regression outcomes for BR at 80 μm, indicating smooth generalization and consistent prediction accuracy

In the Bayesian Regularization (BR) regression analysis for the 80 μm data set, the predictive tendency is more pronounced compared to that for the 40 μm data set. Both the training regression (R = 0.9143) and test regression (R = 0.9337) plots show more compact clustering with less scatter, thus reflecting a higher degree of linear correlation between the predicted and actual densities. However, the all-data regression (R = 0.9122) reaffirms this trend and thereby reveals that the artificial neural network (ANN) is more adept at grasping the inherent dynamics of the 80 μm data compared to the 40 μm data set. The smooth curve with fewer minor deviations implies that the 80 μm data has less variability and higher uniformity within the data, and therefore, the BR approach can learn the function relating the features and the target more accurately.

4.2.3 SC Algorithm

4.2.3.1 For 40 μm

A second algorithm is the Scaled Conjugate Gradient (SCG). It was used on the 40 μm dataset with the same set of three input parameters: the power of the laser beam, the scanning speed, and the frequency for predicting relative density values. Like all other algorithms tested, the dataset (n = 27) was split randomly for training (70%), validation (15%), and testing (15%). The training was stopped after the completion of 25 epochs once the validation criterion was met. As compared to the Levenberg-Marquardt (LM) algorithm, the number of epochs was higher for SCG with stable behavior and signs of no divergence. However, the overall network performance at the end of training is satisfactory with MSE = 0.00993, though slightly inferior compared to the LM algorithm because of the effect of scatter on gradient-based optimization methods.

Table 4.6: Training, validation, and test performance of the SCG-trained ANN for the 40 μm dataset

Dataset	**MSE**	**R**
Training	0.0211	0.9695
Validation	0.0876	0.9224
Test	0.1254	0.9658

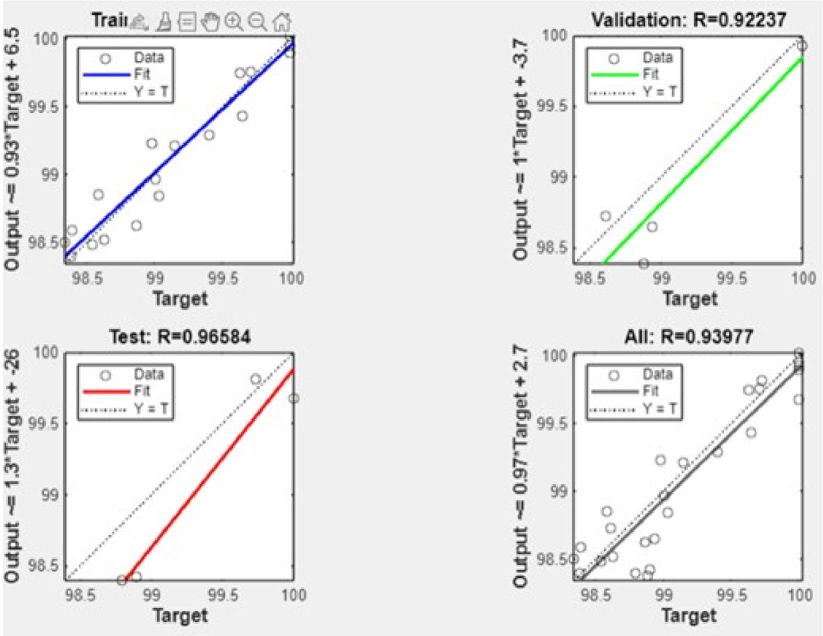

FIGURE 4.5: SCG regression plots for 40 μm dataset, capturing moderate linearity with high test-set correlation

For the 40 μm case, the regression analysis by the SCG learning algorithm determines fair model ability with noticeable variability between the training, validation, and overall data sets. For the training set (R = 0.9695), there is fair linear alignment with a dominant central alignment of all other observed values around the regression function, assuming satisfactory representation of interlinkage between values for the current sub-collection. Additionally, for validation (R = 0.9224), there is fair model generalization ability with noticeable scatter around the regression direction, assuming satisfactory representation of interlinkage between values for the current sub-collection. For the test set (R = 0.9658), there is the best alignment, and it comes closer to being like actual values, which is assumed to be a satisfactory representation of interlinkage between values for the current sub-collection. For the all-data regression (R = 0.9398), the overall alignment is fair with noticeable scatter around the regression direction, assuming a satisfactory representation of interlinkage between values for the current sub-collection. Overall, for this layer thickness, the regression analysis depicts excellent though imperfect consistency in the algorithm behavior.

4.2.3.2 For 80 μm

The Algorithm was again replicated within the 80 μm dataset by training the SCG algorithm with the same three predictor variables. Data splitting was carried out with the standard allocation ratio of 70-15-15. Additionally, the number of training epochs was set at 10 with a validation criterion before the corresponding process for the 40 μm environment.

The final performance with an MSE of 0.0864 depicts that the model was able to capture the general trend from the data well under the increased variability observed for greater layer thicknesses within the L-PBF process.

TABLE 4.7: Training, validation, and testing metrics for the SCG-trained ANN at 80 μm layer thickness

Dataset	MSE	R
Training	0.4108	0.7060
Validation	0.4833	0.9053
Test	0.0664	0.9742

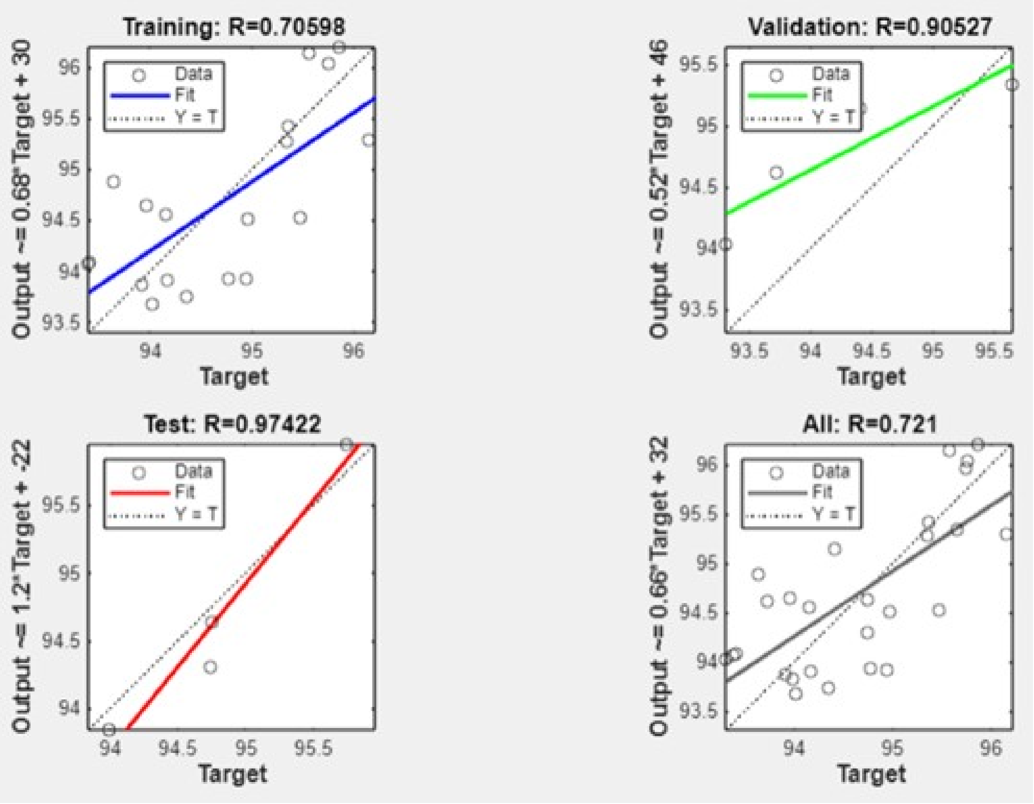

FIGURE 4.6: SCG regression performance for 80 μm showing strong test accuracy despite variability in training data

The regression graphs for the 80 μm dataset scatter with a mixed and understandable performance, with high test performance primarily compared to relatively weaker train and overall data. The train scatter graph (R = 0.7060) shows high scatter and indicates that the model had difficulty capturing all the variability in the 80 μm dataset. On the other hand, the validation scatter (R = 0.9053) showed a much more visible alignment with the target function, with greater generalizability, and unseen instances were more accurate. However, the test scatter graph (R = 0.9742) showed the highest alignment, with a much more visible predicted signal closely aligned with the target function, providing better predictive reliability on unseen instances. On the other hand, the overall data regression (R = 0.721) showed much higher variability, with noise and nonlinear interactions incompletely modeled by the available SCG algorithm. Overall, the current method is adequately and indefinitely inefficient for the current 80 μm dataset.

4.3 Regression and Response-Surface Analysis

4.3.1 40 μm Layer Thickness

In the statistical analysis, factor A represents laser power, factor B represents scanning speed, and factor C represents pulse frequency. The contour graphs in Figure 4-7 for LT of 40 μm show how the relative density varies when two variables are changed, with the third variable fixed at the central nominal level ($P = 160$ W, $v = 550$ mm/s, $f = 6$ Hz). For the P–v plane, the density is found to attain the highest level for intermediate P and lower v, dropping off as v is raised, hence affirming that higher speeds of travel will negatively affect the consolidation process. The P–f plane highlights that the loss of density is large with the increase of f, with P showing less effect, also consistent with the regression analysis that ranked f as having the largest variances. Lastly, the f–v plane suggests high sensitivity for the variable f, with lower sensitivity for v, hence indicating f as the dominant variable for control purposes when the sample distance is 40 μm.

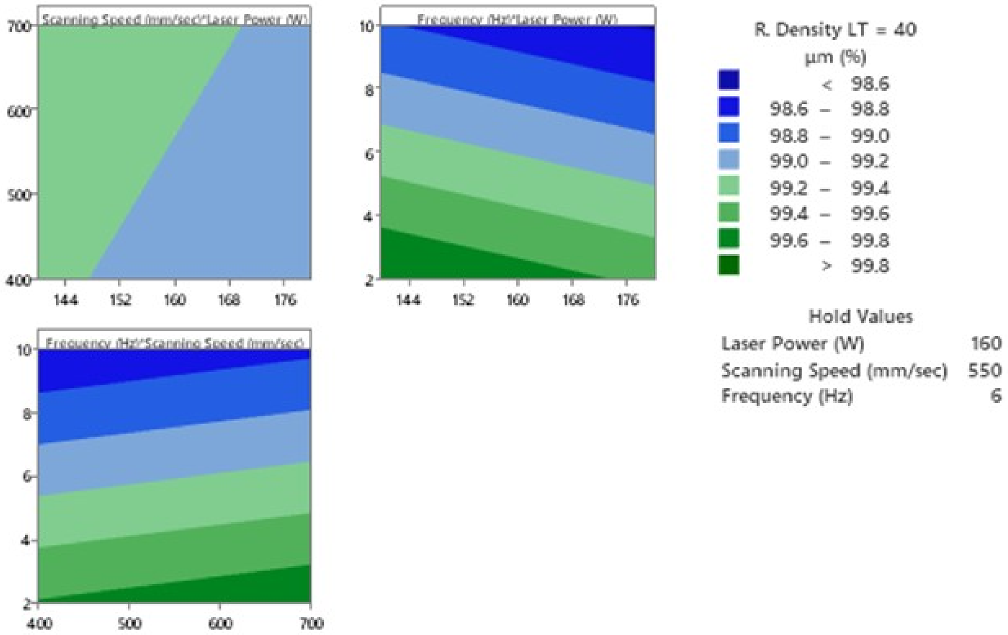

Figure 4.7: Contour plots of relative density at LT = 40 μm (%) as a function of (a) laser power vs. scanning speed, (b) laser power vs. frequency, and (c) scanning speed vs. frequency, with the third factor held at its center level

The Pareto chart in Figure 4.8 highlights the normalized effects of every term involved in the response surface regression equation for the 40 μm data. The main term for frequency (C) and the quadratic terms of C^2/CC well exceed the 95% significance level (marked by the vertical red line at about 2.11), implying that the linear and nonlinear effects of the parameter of frequency make significant, large impacts on the density.

The other terms, including the interaction terms of the variables of laser power (A) and scanning speed (B), do not exceed the significance level, indicating that these parameters make only marginal impacts. The ANOVA results and the Pareto chart consistently identify pulse frequency as the dominant factor controlling relative density at 40 μm.

This response surface, shown in Figure 4.9, helps illustrate the interaction of the effects of the frequency and the laser power on the relative density when LT is at 40 μm, along with the scanning speed held constant at 550 mm/s. Concerning the surface, there is a steep gradient concerning the frequencies, suggesting that there is a gradual reduction of the density with the increase of the frequencies from the lower level to the higher level. However, the gradient of the surface concerning

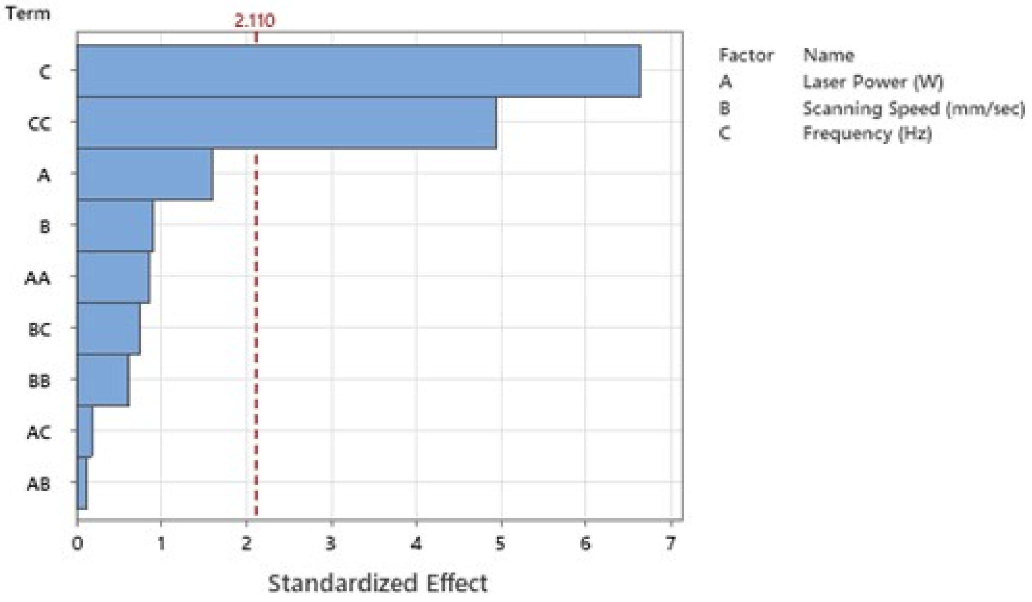

FIGURE 4.8: Pareto chart of standardized regression effects for R. Density LT = 40 μm (%), showing frequency and its quadratic term as the only statistically significant contributors ($\alpha = 0.05$).

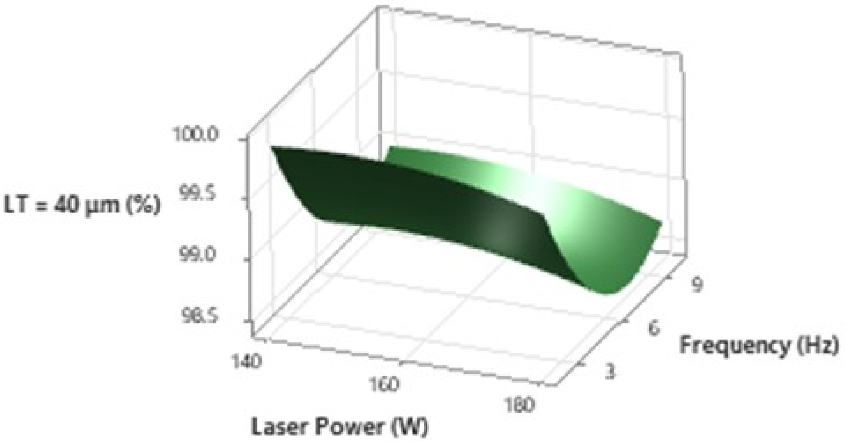

FIGURE 4.9: Response surface of R. Density LT = 40 μm (%) as a function of frequency and laser power at fixed scanning speed (v = 550 mm/s), highlighting the dominant effect of frequency

the laser power is shallow, suggesting that the secondary variable that affects the density is laser power. Additionally, the surface is less curved, indicating that there is a large quadratic term concerning the frequencies, which was detected by the regression analysis.

The response surface for LT = 40 μm in Figure 4.10 illustrates the relative density, which varies with the frequency and the scanning speed, for a fixed laser power

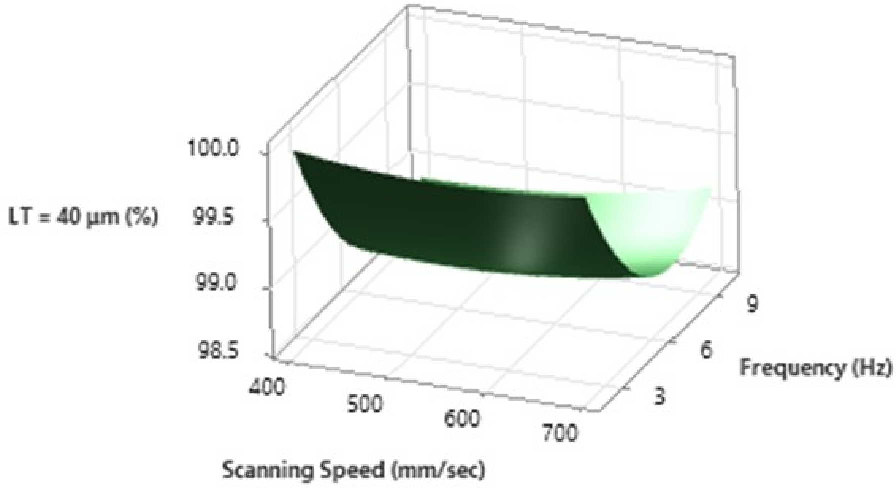

FIGURE 4.10: Response surface of R. Density LT = 40 μm (%) versus frequency and scanning speed at fixed laser power (P = 160 W), showing frequency as the primary control variable

of 160 W. As per the previous observation, the gradient of the surface is large along the frequency axis, where the density decreases with the increase of the frequencies, and the other variable, the scanning speed, is less prominent. The surface is tilted, along the scanning speed, meaning that with the higher speeds, there will be a slight reduction in the density. However, the dominant factors are not the scanning speeds. Overall, it depicts a large flat area of high density at lower frequencies for varying scanning speeds, consistent with the small, standardized difference observed for the scanning speed in the Pareto chart, meaning that the dominant variable among the three for high density is the frequency.

The last response surface shown in Figure 4-11 is for the interaction of the laser power and the scanning speed when the LT is 40 μm, with a frequency of 6 Hz. The surface reveals that the density of the material is at its highest when the interaction of the laser power and the scanning speed is at a middle level, where the higher scanning speed results in decreased density. The interaction surface for the variables of the laser power is less steep compared with the other variables, indicating that the main effect of the variable of the laser power is less steep than the other variables. This plot explains the trade-off between the variables of the laser power and the scanning speed, showing that although they affect the density, their effects are secondary compared with the effects of the variable

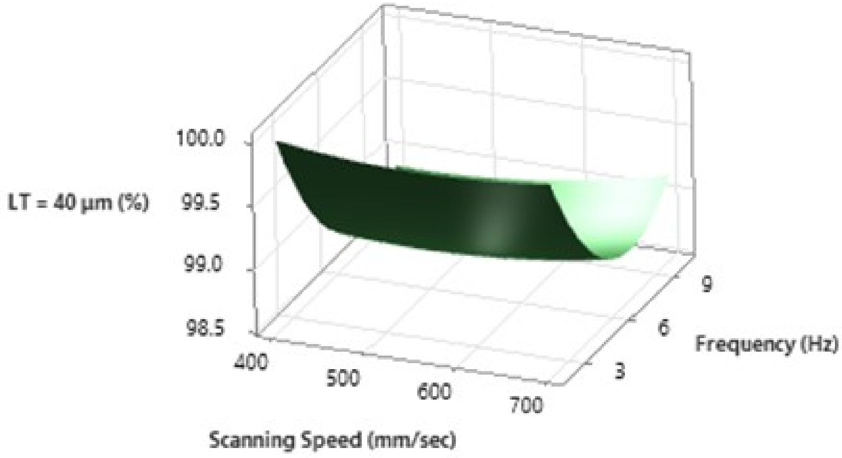

FIGURE 4.11: Response surface of R. Density LT = 40 μm (%) as a function of laser power and scanning speed at fixed frequency (f = 6 Hz), illustrating a moderate trade-off between energy input and relative density

of the frequency. Analysis of variance (ANOVA) was performed to determine the statistical significance of the process parameters affecting relative density at 40 μm layer thickness. The ANOVA results showed that the overall regression model was statistically significant ($p < 0.001$), with the model accounting for 81.31% of the total variation in response. Among the linear terms, pulse frequency was the dominant factor, contributing to 48.79% of the total variation and showing a highly significant effect ($p < 0.001$). The quadratic terms were also significant ($p = 0.001$), mainly because of the strong contribution of the frequency-squared term, whereas laser power and scanning speed were not individually significant within the investigated range. The two-way interaction terms were statistically insignificant ($p = 0.888$), indicating that the 40 μm response was governed mainly

TABLE 4.8: Summary of ANOVA results for the 40 μm relative-density dataset

Term	**Contribution (%)**	**F-value**	**P-value**	**Interpretation**
Model	81.31	8.22	0.000	Significant
Laser power	2.83	2.57	0.127	Not significant
Scanning speed	0.90	0.82	0.377	Not significant
Frequency	48.79	44.37	0.000	Significant
Quadratic terms	28.10	8.52	0.001	Significant
Two-way interactions	0.69	0.21	0.888	Not significant

by pulse frequency and nonlinear curvature rather than by interaction-dominated behaviour.

4.3.2 80 μm Layer Thickness

The Pareto chart shown in Figure 4.12 for the 80 μm dataset indicates that pulse frequency is the dominant factor affecting relative density and is the only parameter that clearly exceeds the statistical significance threshold. Laser power and scanning speed exhibit comparatively smaller standardized effects, indicating weaker influence within the investigated process range. The subsequent response-surface plots also show that the strongest density variation occurs along the pulse-frequency direction, particularly at higher layer thickness.

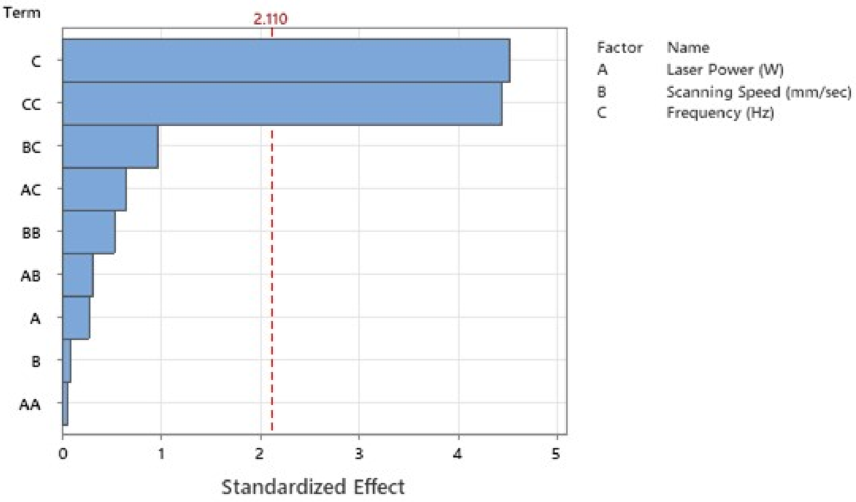

FIGURE 4.12: Pareto chart of standardized effects for 80 μm layer thickness showing frequency and its quadratic term as dominant contributors to relative density

This surface plot reveals a significant reduction in relative density with the rising frequency, indicating a strong negative effect of the oscillation frequency on melt pool stability at a layer thickness of 80 μm, as shown in Figure 4.13. The changes in the densities for varying laser powers are less significant, indicating only a weak effect in the given range. The terrain of the surface plot reveals a non-linear relationship where higher frequencies, along with higher powers, accelerate the creation of pores. This is not unexpected for LPBF, considering the commonly reported instabilities for higher layers.

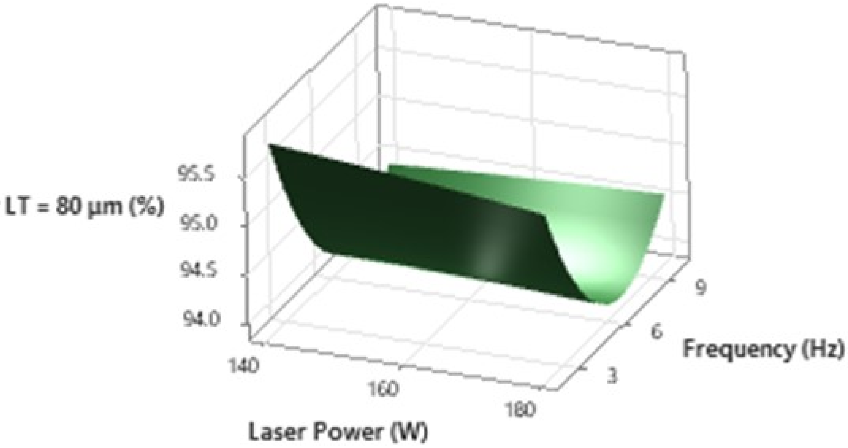

FIGURE 4.13: Response surface for R. Density at 80 μm showing the combined effect of laser power and frequency (scanning speed held at 550 mm/s)

The plot in Figure 4.14 highlights the coupled effects of frequency and scanning speed, along with the effects of the melt density, showing a sharp decrease with increasing frequencies, independent of scanning speed. Scanning speed affects the curvature, where lower speeds induce higher compaction, and higher speeds reduce the melt stability. The melt pool thinning, along with the reduced fusion of the thicker layers, is indicated by the basin-shaped curvature of the high frequencies.

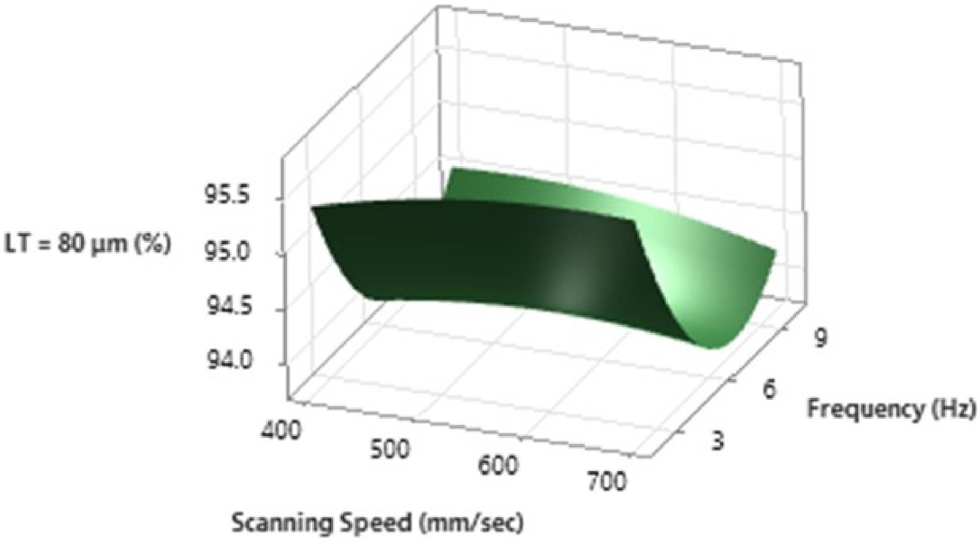

FIGURE 4.14: Response surface for R. Density at 80 μm as a function of scanning speed and frequency (laser power = 160 W)

This surface reveals a small degree of curvature with respect to scanning speed and laser power, suggesting that both factors affect heat input, but less than the frequency, as shown in Figure 4.15. The higher scanning speeds result in lower densities because of reduced melt-pool residence times, and the higher laser powers counter the effects of higher speeds by increasing the melt pool size. This surface curvature is consistent with the typical energy balancing that happens during LPBF processes for thicker layers. In the statistical analysis, factor A represents laser power, factor B represents scanning speed, and factor C represents pulse frequency. Analysis of variance (ANOVA) was also performed for the 80 μm relative-density dataset to evaluate the significance of the selected process parameters. The regression model was statistically significant ($p = 0.018$). Among the linear factors, pulse frequency was the only statistically significant term, contributing 34.67% of the total variation and producing the highest F-value among the examined parameters. In contrast, laser power and scanning speed showed negligible contributions and were not statistically significant within the investigated range. These findings indicate that relative density at 80 μm was governed primarily by pulse frequency, while the effects of laser power and scanning speed were comparatively weaker within the selected process window.

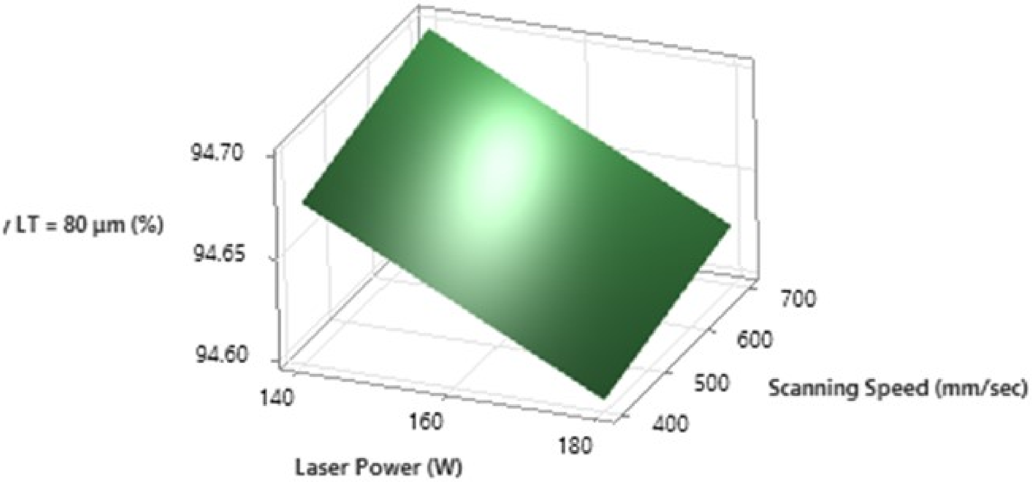

Figure 4.15: Response surface for R. Density at 80 µm showing interaction between scanning speed and laser power (frequency held at 6 Hz)

Table 4.9: Summary of ANOVA results for the 80 μm relative-density dataset

Term	Contribution (%)	F-value	P-value	Interpretation
Regression model	34.81	4.09	0.018	Significant
Laser power	0.13	0.04	0.835	Not significant
Scanning speed	0.01	0.00	0.947	Not significant
Frequency	34.67	12.23	0.002	Significant

4.4 ANN Predictions vs Experimental Values

4.4.1 ANN Results for 40 μm Layer Thickness

In the case of the 40 μm image analysis, all three artificial neural network (ANN) training algorithms: Levenberg-Marquardt (LM), Bayesian Regularization, and Scalable Conjugate Gradient (SCG), showed considerable predictive power, though with varying levels of accuracy. The experimental volume densities ranged from 97.77% to 99.17%, and the ANN outputs tracked them well. In this case, the best predictive results were obtained with the LM method, with a test correlation of $R = 0.9098$ and prediction errors mostly below $\pm 0.15\%$. Bayesian model predictions were smoother, though slightly less accurate, and represented typical regularization behavior, with moderate scatter and very high test correlations ($R = 0.9658$) for SCG.

Across the dataset, the ANN tended to under-predict at higher density ($> 99\%$) and showed small amounts of over-prediction at moderate volumetric energy density (VED). This is consistent with the nonlinear consolidation observed during LPBF. Small amounts of over-prediction were observed under moderate volumetric energy density (VED) conditions.

In general, the ANN ensemble reproduced the statistical and physical properties well during the 40-μm LPBF process. The strong correlation between the ANN-predicted and actual values provides evidence for the high learnability of this thickness range with fewer thermal gradients and more consistent layer compaction. The above finding can be regarded as direct validation of the recalculation process for VED/BED based on ANN MSE.

4.4.2 ANN Results for 80 μm Layer Thickness

For the 80 μm dataset, densities were overall lower and more varied, ranging from 95.47% to 97.35%. For all artificial neural network (ANN) models, the trend was observed; however, with reduced energy absorption efficiency at higher layer thicknesses. Once again, the Levenberg-Marquardt (LM) algorithm performed best with $R = 0.9865$ on the test set, better than for the 40 μm dataset, and thus showed excellent generalization ability after training. Bayesian Regularization produced a good correspondence between the function and the data ($R = 0.9337$), and for Scaled Conjugate Gradient (SCG), the training scatter was again the largest, with excellent test correlation ($R = 0.9742$).

Under-prediction was observed in the sample, with more frequent under penetration and lack-of-fusion defects in builds with a layer thickness of 80 μm. Over-prediction was observed within the mid-Volume Energy Density (VED) range, indicating the model's tendency to predict greater consolidation than is realistically possible in higher layers. This is consistent with known principles of LPBF processes, in which higher layers promote greater thermal gradients and lower volume absorption.

Despite these difficulties, all ANN approaches maintained errors at a suitable level and preserved the trend's direction. The natural variability in layer thicknesses of 80 μm made this test case more informative for the strength and validity of ANN approaches and explains the relevance of recalculating with MSE for the parameter VED/BED. In this way, this investigation realistically accounts for process variability in LPBF processes, unlike traditional approaches for calculating VED.

4.5 Volumetric Energy Density Results

This section compares the experimental volumetric energy density values used as reference with the ANN-adjusted VED values obtained using the three ANN training algorithms. The objective is to assess how incorporation of ANN prediction error modifies the energy-density interpretation for the 40 μm and 80 μm datasets. The comparison is presented separately for each layer-thickness condition because the ANN models were trained independently for the two datasets.

4.5.1 Original Volumetric Energy Density from Literature

The experimental VED values listed in this study were used as the baseline reference for comparison with ANN-adjusted VED values. These reference values are presented separately for the 40 μm and 80 μm datasets in the comparison tables. Higher experimental VED values are generally associated with combinations involving higher laser power and lower scanning speed, whereas lower VED values correspond to lower power and/or faster scan conditions. These baseline values provide the theoretical energy-input reference against which the ANN-adjusted results were assessed.

4.5.2 ANN-Adjusted Volumetric Energy Density Based on MSE

The ANN-normalized values for VED indicate observable and interpretable differences in comparison to the raw EXP VED values. Starting with a thickness of 40 µm for a single layer, variations between EXP VED and ANN VED for each of the three ANN approaches appear small. This can be considered logical because melting pool stability and compactness properties are more consistent for smaller layers. Among the approaches for optimizing ANN training used in this study, the LM algorithm always tends towards values closest to those of EXP VED. This clearly indicates low adjustment requirements and thus a high degree of confidence about predictions. The SCG approach brings about a modest adjustment in values.

TABLE 4.10: Selected-case comparison of experimental and ANN-adjusted VED for the parameter set $P = 140$ W, $v = 400$ mm/s, $f = 2$ kHz at 40 μm layer thickness

Parameter	Value
Laser Power (W)	140
Scanning Speed (mm/s)	400
Pulse Frequency (kHz)	2
Exp. VED	6.25700×10^{-9}
LM VED	6.29555×10^{-9}
SCG VED	6.35875×10^{-9}
BR VED	6.66247×10^{-9}

TABLE 4.11: Selected-case comparison of experimental and ANN-adjusted VED for the parameter set $P = 140$ W, $v = 400$ mm/s, $f = 2$ kHz at 80 μm layer thickness

Parameter	Value
Laser Power (W)	140
Scanning Speed (mm/s)	400
Pulse Frequency (kHz)	2
Exp. VED	6.25700×10^{-9}
LM VED	6.59417×10^{-9}
SCG VED	6.58810×10^{-9}
BR VED	6.66024×10^{-9}

For illustration, Tables 4.10 and 4.11 present a selected parameter case to compare the experimental VED with the ANN-adjusted VED values obtained using LM, SCG, and BR for the 40 μm and 80 μm datasets, respectively. This example highlights how the same nominal parameter set leads to different adjusted energy interpretations depending on layer thickness and ANN training algorithm.

The values for Bayesian Regulation appear smoother but somewhat higher due to regularization for possible weight adjustment outstanding. For the 40 μm dataset, the comparison between experimental and ANN-adjusted VED values is presented in Table 4.12, while the corresponding comparison for the 80 μm dataset is given in Table 4.13. The differences between these values indicate how strongly each ANN model modifies the interpretation of energy input relative to the experimental reference.

Table 4.12: Comparison of experimental VED values and ANN-adjusted VED outputs for 40 μm layer thickness using LM, SCG, and Bayesian training algorithms

SR	EXP VED (40 μm)	LM ANN VED	SCG ANN VED	Bayes ANN VED
1	4.07739×10^{-8}	4.10755×10^{-8}	4.14866×10^{-8}	4.11932×10^{-8}
2	2.63154×10^{-9}	2.65077×10^{-9}	2.67699×10^{-9}	2.65882×10^{-9}
3	6.25700×10^{-9}	6.29555×10^{-9}	6.35875×10^{-9}	6.66247×10^{-9}
4	1.00571×10^{-8}	1.01351×10^{-8}	1.02328×10^{-8}	1.06647×10^{-8}
5	2.33226×10^{-8}	2.34398×10^{-8}	2.37255×10^{-8}	2.49143×10^{-8}
⋮	⋮	⋮	⋮	⋮
27	1.67994×10^{-8}	1.74441×10^{-8}	1.76076×10^{-8}	1.78084×10^{-8}

For a thickness of 80 μm, a larger deviation of ANN VED values can be observed with respect to the EXP curve. This deviation shows more pronounced physical variations for thicker layers, where lower efficiency of absorption, increased values of thermal gradients, and imprecision in melt pool creation led to more prominent ANN uncertainty. Therefore, more prominent adjustments of values for ANN models, specifically for the Bayesian model, can be observed, basically showing that a lower VED understates the actual energy needs for realizing similar levels of densification for a thickness of 80 μm. The LM model again approaches EXP more but sustains differences. In other words, ANN-adjusted VED realistically describes energy use based on physical laws while accurately expressing subtle losses that cannot be modelled by EXP VED.

Table 4.13: Comparison of experimental VED values and ANN-adjusted VED predictions for 80 μm layer thickness across all three ANN algorithms

SR	EXP VED (80 μm)	LM ANN VED	SCG ANN VED	Bayes ANN VED
1	4.2085×10^{-8}	4.25240×10^{-8}	4.24839×10^{-8}	4.29647×10^{-8}
2	2.7373×10^{-9}	2.76566×10^{-9}	2.76307×10^{-9}	2.79421×10^{-9}
3	6.5267×10^{-9}	6.59460×10^{-9}	6.58841×10^{-9}	6.66274×10^{-9}
4	1.0467×10^{-8}	1.05769×10^{-8}	1.05668×10^{-8}	1.06874×10^{-8}
5	2.4405×10^{-9}	2.46590×10^{-9}	2.46358×10^{-9}	2.49143×10^{-9}
⋮	⋮	⋮	⋮	⋮
27	1.74441×10^{-8}	1.76244×10^{-8}	1.76076×10^{-8}	1.78084×10^{-8}

4.6 Percentage Deviation Analysis

This section examines the percentage deviation between the experimental VED values and the ANN-adjusted VED values for the 40 μm and 80 μm datasets. The aim is to assess how sensitive the recalculated energy descriptor is to ANN prediction error for each training algorithm. Separate deviation plots were generated for each thickness condition to compare the stability of the LM, BR, and SCG models.

The percentage deviation was calculated for all 27 experimental samples using:

$$\%\text{Deviation} = \frac{\text{EXP VED} - \text{ANN VED}}{\text{EXP VED}} \times 100 \tag{4.1}$$

Separate scatter plots were generated for each thickness to visualize and compare the predictive stability of the ANN models.

4.6.1 Deviation Analysis at 40 μm Layer Thickness

For the 40 μm dataset, the percentage deviations remained small for all three ANN algorithms, indicating a high level of consistency between the experimental and ANN-adjusted VED values. The deviation ranges were approximately 1.01–1.03% for LM, 0.72–0.74% for SCG, and 1.72–1.75% for BR. The deviation trends for all 27 samples are shown in Figure 4.16. Among the three algorithms, SCG produced the smallest deviation band for the 40 μm case, followed by LM, while BR showed slightly larger but still stable deviations due to regularization effects.

Examples with larger deviation values are:

- LM: samples 8, 14 & 27 showing minor peaks around ∼1.03%.
- SCG: samples 8, 14, 27 showing values around ∼0.74%.

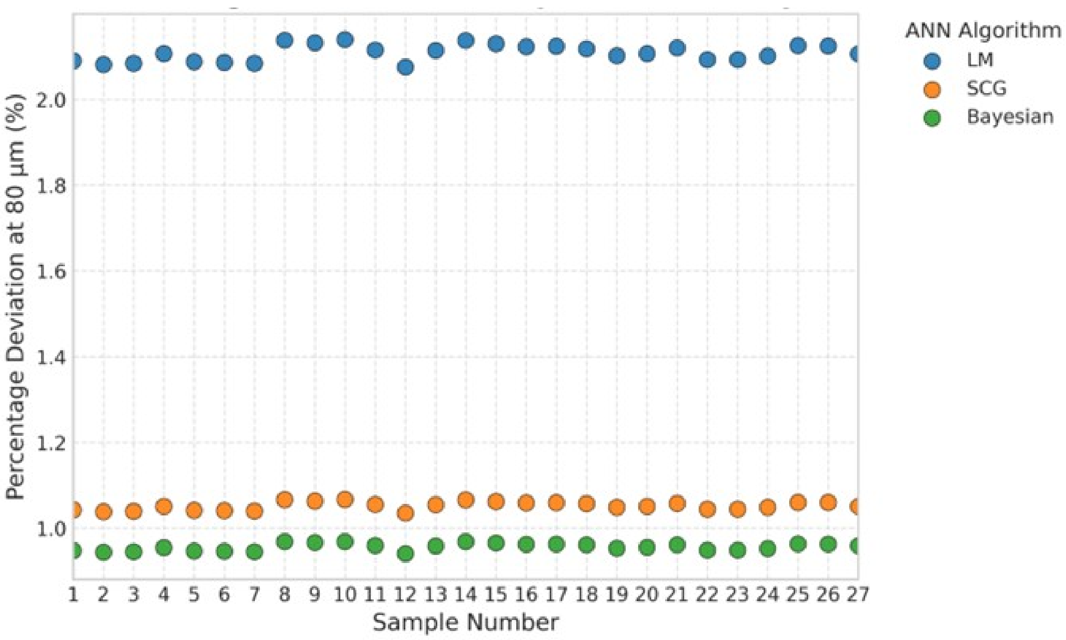

FIGURE 4.16: Percentage deviation between ANN-predicted and experimental VED values for 40 μm layer thickness using LM, SCG, and Bayesian ANN algorithms

- Bayesian: samples 8, 14, 27 with the most significant relative values around 1.75%. The values are small with no outliers. This indicates a perfect generalization for the ANN models.

The values are small with no outliers. This indicates a perfect generalization for the ANN models.

4.6.2 Deviation Analysis at 80 μm Layer Thickness

For the 80 μm dataset, the percentage deviations were again stable, although the spread differed among the three ANN algorithms. The LM algorithm showed deviations of approximately 2.08–2.14%, SCG showed deviations of approximately 1.03–1.07%, and BR produced the lowest overall deviation range of about 0.94–0.97%. The corresponding trend plot is shown in Figure 4.17. These results indicate that, for the 80 μm condition, BR provided the most consistent ANN-adjusted VED values relative to the experimental reference, whereas LM showed the largest correction range.

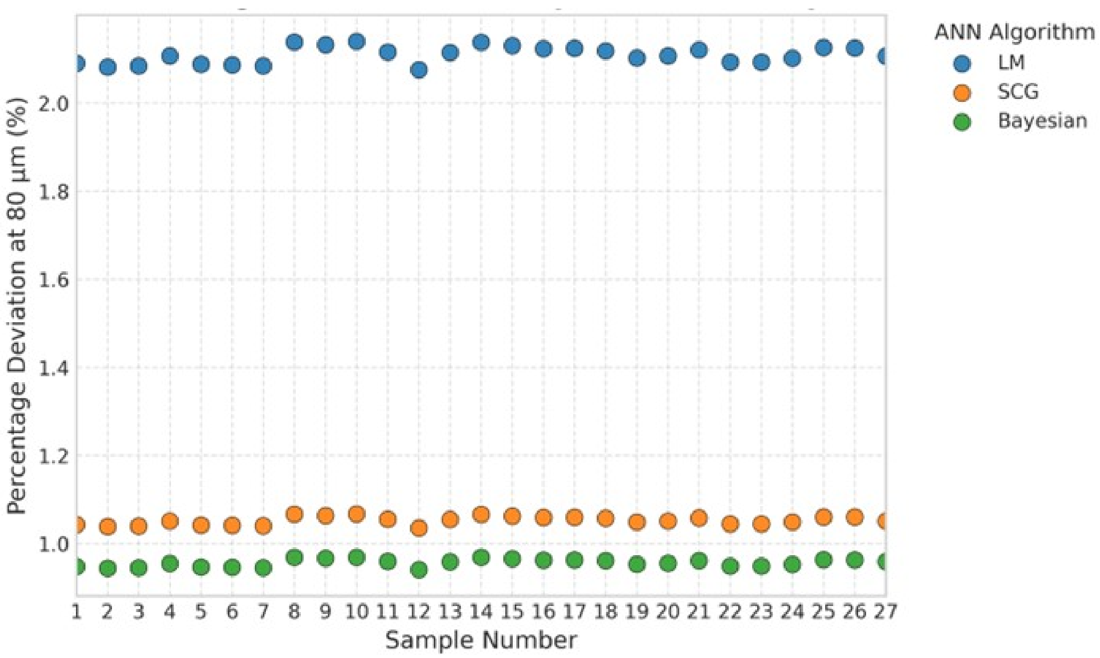

FIGURE 4.17: Percentage deviation between ANN-predicted and experimental VED values for 80 μm layer thickness using LM, SCG, and Bayesian algorithms

Situations where deviation was relatively higher were recorded in the following samples:

- LM: samples 7, 11, and 25, deviations about 2.13% to 2.14%.
- SCG: samples 7, 14, and 27; deviation of ∼1.07%.
- Bayesian: increments in samples 7, 14, and 25 with variations about 0.96%–0.97%.

In general, the stability of the ANN results for 80 μm resolution is exceptional, with deviation curves showing slight oscillation and no signs of fluctuations in predictions.

4.7 Comparative Discussion

A comparative assessment of the three ANN training algorithms shows that the Levenberg–Marquardt (LM) method provided the strongest overall predictive performance for relative density, particularly in terms of convergence behaviour and test-set correlation. However, the algorithm producing the best density prediction was not always the one yielding the lowest deviation in recalculated VED. For the 40 μm dataset, the lowest deviation in ANN-adjusted VED was obtained with SCG, whereas for the 80 μm dataset the lowest deviation was obtained with Bayesian Regularization (BR). This indicates that density-prediction accuracy and stability of energy-descriptor adjustment are related but not identical aspects of model performance.

Comparison of the two layer-thickness conditions also shows that the 40 μm dataset exhibited greater stability and narrower deviation bands, whereas the 80 μm dataset was more sensitive to ANN prediction error and showed greater variation in recalculated VED behaviour. This suggests that thicker layers are associated with more complex process response and stronger sensitivity of the energy-based interpretation to modelling uncertainty.

The statistical analysis further supports this interpretation. ANOVA, Pareto, and response-surface analysis consistently identified pulse frequency as the dominant factor affecting relative density within the investigated parameter range. Laser power and scanning speed had comparatively smaller effects, although they still contributed to the overall response behaviour. For the 40 μm dataset, the response also showed a notable nonlinear contribution associated with the frequency-squared term, while the 80 μm dataset remained primarily governed by the dominant effect of frequency.

Overall, the combined ANN and statistical results indicate that pulse frequency was the main control variable in the present NiTi L-PBF dataset, and that incorporation of ANN prediction error into VED/BED analysis provides a more informative basis for process interpretation than a static energy-density descriptor alone.

Chapter 5

Conclusion and Future Recommendations

5.1 Conclusion

The present study developed and evaluated an ANN-based framework for analysing the influence of Laser Powder Bed Fusion (L-PBF) process parameters on the relative density of NiTi alloy, while also examining how prediction error can be incorporated into the interpretation of volumetric energy density. Using a literature-derived dataset consisting of 27 unique parameter combinations of laser power, scanning speed, and pulse frequency, with relative-density values reported for 40 μm and 80 μm layer-thickness conditions, the work treated the two thickness levels as separate datasets for modelling and comparison. Three ANN training algorithms, namely Levenberg–Marquardt (LM), Scaled Conjugate Gradient (SCG), and Bayesian Regularization (BR), were implemented in MATLAB, while Minitab was used for ANOVA, Pareto, and response-surface analyses.

The results showed that the LM algorithm provided the strongest overall predictive performance for relative density, whereas the lowest deviation in recalculated VED was obtained with SCG for the 40 μm dataset and with BR for the 80 μm dataset. This indicates that the algorithm producing the best density prediction is not necessarily the one giving the lowest deviation in the adjusted energy-density formulation. Comparative analysis further showed that the 40 μm condition exhibited greater stability and lower deviation, while the 80 μm condition was more sensitive to prediction error and displayed more complex process behaviour. These findings suggest that thicker layers are associated with greater variability in process response and energy-based interpretation.

The statistical analysis supported the ANN results and improved the interpretation of parameter sensitivity. ANOVA and Pareto analysis showed that pulse frequency was the dominant factor affecting relative density, especially for the 40 μm dataset, while laser power and scanning speed had comparatively smaller effects within the investigated parameter range. For the 40 μm condition, the analysis also indicated an important nonlinear contribution associated with the quadratic frequency effect, whereas the 80 μm condition remained primarily governed by the linear effect of frequency. The response-surface plots further confirmed that changes in density were most strongly associated with variation in pulse frequency.

Overall, the study demonstrates that incorporating ANN prediction error into the recalculation of VED/BED provides a more informative framework than relying on a static energy-density descriptor alone. Rather than using ANN only as a predictive tool, the proposed approach links model uncertainty to process interpretation and offers an additional basis for evaluating L-PBF parameter behaviour. Although the dataset size was limited and the results should therefore be interpreted as exploratory, the framework provides a useful proof of concept for integrating data-driven modelling with statistical analysis in NiTi L-PBF research.

5.2 Future Work

Given the limited dataset size, the resulting performance metrics are sensitive to the selected partition. Accordingly, the ANN results in this study should be interpreted as exploratory and proof-of-concept in nature. Future work should employ repeated random sub-sampling, k-fold cross-validation, or leave-one-out validation, and should compare ANN performance with alternative small-data regression methods such as Gaussian Process Regression or response-surface models. Though this framework properly connects ANN prediction quality with energy density concepts for L-PBF based on artificial neural networks (ANNs), some significant developments are also required for this model to be considered a general optimization tool. This model used a relatively small data set of a single material based on published NiTi experiments. Future studies should focus on multi-material data with more machines and larger parameter variations (covering a range of scanning methods and layer sizes) to check transferability for ANN-adjusted volumetric energy density (VED). A larger input variable field, encompassing powder properties, building orientations, and pre/post-process heat treatments, would add more physical importance to this model.

Second, modifications in the architecture of the artificial neural network (ANN) may be achieved. A different design of neural networks, like physics-informed neural networks, or maybe Bayesian neural networks, may provide more explicit estimates of uncertainty than the simple use of Mean Squared Error (MSE). This uncertainty might then be propagated within the Variational Energy Density (VED) theory using more sophisticated probabilistic frameworks to provide confidence bands for energy density windows instead of a corrected estimate. Also, integration with optimization techniques (like Genetic Algorithms or Bayesian Optimization) would help in autonomously finding parameter values that give optimal results with minimal deviation while being bound by density and productivity conditions.

A third approach may be to integrate data such as melt pool images, pyrometry measurements, and/or acoustic emissions directly with ANN-VED to extend this tool in a more realistic manner towards a closed loop. Real-time deviation maps might be utilized to dynamically adjust power and/or feed rate during a print to put a practical face to the idea of energy density. Furthermore, comparison of this new approach with experimental data generated in-house for validation purposes would replace comparison with literature values for a strengthened experimental basis. Altogether, this would transform the current proof-of-concept stage towards a strong generalizable tool for brilliant parameter selection in metal additive manufacturing.

Bibliography

[1] A. Alfaify, M. Saleh, F. M. Abdullah, and A. M. Al-Ahmari, “Design for additive manufacturing: A systematic review,” *Sustainability*, vol. 12, no. 19, p. 7936, 2020.

[2] L. Zhou, J. Miller, J. Vezza, M. Mayster, M. Raffay, Q. Justice, Z. Al Tamimi, G. Hansotte, L. D. Sunkara, and J. Bernat, “Additive manufacturing: a comprehensive review,” *Sensors*, vol. 24, no. 9, p. 2668, 2024.

[3] J. Pasco, Z. Lei, and C. Aranas Jr, “Additive manufacturing in off-site construction: review and future directions,” *Buildings*, vol. 12, no. 1, p. 53, 2022.

[4] T. Feldhausen, L. Heinrich, K. Saleeby, A. Burl, B. Post, E. MacDonald, C. Saldana, and L. Love, “Review of computer-aided manufacturing (cam) strategies for hybrid directed energy deposition,” *Additive Manufacturing*, vol. 56, p. 102900, 2022.

[5] Additive Manufacturing Research Group, Loughborough University, “Material extrusion,” 2025. Accessed: February 04, 2026.

[6] Z. U. Arif, M. Y. Khalid, R. Noroozi, M. Hossain, H. H. Shi, A. Tariq, S. Ramakrishna, and R. Umer, “Additive manufacturing of sustainable biomaterials for biomedical applications,” *Asian Journal of Pharmaceutical Sciences*, vol. 18, no. 3, p. 100812, 2023.

[7] Additive Manufacturing Research Group, Loughborough University, “Vat photopolymerisation,” 2026. Accessed: Mar. 25, 2026.

[8] Additive Manufacturing Research Group, Loughborough University, “Powder bed fusion,” 2025. Accessed: February 04, 2026.

[9] S. L. Sing and W. Y. Yeong, "Laser powder bed fusion for metal additive manufacturing: perspectives on recent developments," *Virtual and Physical Prototyping*, vol. 15, no. 3, pp. 359–370, 2020.

[10] S. L. Sing, S. Huang, G. D. Goh, G. L. Goh, C. F. Tey, J. H. K. Tan, and W. Y. Yeong, "Emerging metallic systems for additive manufacturing: In-situ alloying and multi-metal processing in laser powder bed fusion," *Progress in Materials Science*, vol. 119, p. 100795, 2021.

[11] J. Wang, R. Zhu, Y. Liu, and L. Zhang, "Understanding melt pool characteristics in laser powder bed fusion: An overview of single-and multi-track melt pools for process optimization," *Advanced Powder Materials*, vol. 2, no. 4, p. 100137, 2023.

[12] P. Ninpetch, P. Kowitwarangkul, S. Mahathanabodee, P. Chalermkarnnon, and P. Ratanadecho, "A review of computer simulations of metal 3d printing," in *AIP Conference Proceedings*, vol. 2279, p. 050002, AIP Publishing LLC, 2020.

[13] F. Aguilar, T. Huynh, N. Kljestan, M. Knezevic, and Y. Sohn, "Microstructure and mechanical characterization of aisi 4340 steel additively manufactured by laser powder bed fusion," *Metals*, vol. 15, no. 4, p. 412, 2025.

[14] A. Dareh Baghi, S. Nafisi, R. Hashemi, H. Ebendorff-Heidepriem, and R. Ghomashchi, "A new approach to empirical optimization of laser powder bed fusion process for ti6al4v parts," *Journal of Materials Engineering and Performance*, vol. 32, no. 20, pp. 9472–9488, 2023.

[15] M. Gor, H. Soni, V. Wankhede, P. Sahlot, K. Grzelak, I. Szachgluchowicz, and J. Kluczyński, "A critical review on effect of process parameters on mechanical and microstructural properties of powder-bed fusion additive manufacturing of ss316l," *Materials*, vol. 14, no. 21, p. 6527, 2021.

[16] D. Wang, L. Liu, J. Tang, Y. Liu, C. Wei, Z. Weng, J. Shao, H. Tan, W. Zhou, B. Neirinck, *et al.*, “Recent advances on additive manufacturing of heterogeneous/gradient metallic materials via laser powder bed fusion,” *International Journal of Extreme Manufacturing*, vol. 7, no. 6, p. 062007, 2025.

[17] M. Taghian, M. H. Mosallanejad, E. Lannunziata, G. Del Greco, L. Iuliano, and A. Saboori, “Laser powder bed fusion of metallic components: Latest progress in productivity, quality, and cost perspectives,” *Journal of Materials Research and Technology*, vol. 27, pp. 6484–6500, 2023.

[18] E. Ghio and E. Cerri, “Additive manufacturing of alsi10mg and ti6al4v lightweight alloys via laser powder bed fusion: a review of heat treatments effects,” *Materials*, vol. 15, no. 6, p. 2047, 2022.

[19] K. Karami, A. Blok, L. Weber, S. Ahmadi, R. Petrov, K. Nikolic, E. Borisov, S. Leeflang, C. Ayas, A. Zadpoor, *et al.*, “Continuous and pulsed selective laser melting of ti6al4v lattice structures: Effect of post-processing on microstructural anisotropy and fatigue behaviour,” *Additive Manufacturing*, vol. 36, p. 101433, 2020.

[20] R. Joch, M. Šajgalík, M. Drbúl, D. Měřínska, J. Markovič, and A. Czán, “Impact of powder bed fusion printing process parameters on the achieved quality of pa12 manufactured parts,” *Progress in Additive Manufacturing*, pp. 1–19, 2025.

[21] H. Zhang, B. Song, K. Shi, Y. Chen, B. Yang, M. Chang, L. Hu, J. Xing, and D. Gu, “Rapid optimization of laser powder bed fusion process: a high-throughput integrated multi-task robust modeling approach,” *International Journal of Extreme Manufacturing*, vol. 7, no. 4, p. 045005, 2025.

[22] J. Wang, R. Zhu, Y. Liu, and L. Zhang, “Understanding melt pool characteristics in laser powder bed fusion: An overview of single-and multi-track melt pools for process optimization,” *Advanced Powder Materials*, vol. 2, no. 4, p. 100137, 2023.

[23] A. Marques, A. Cunha, M. R. Silva, M. I. Osendi, F. S. Silva, O. Carvalho, and F. Bartolomeu, "Inconel 718 produced by laser powder bed fusion: an overview of the influence of processing parameters on microstructural and mechanical properties," *The International Journal of Advanced Manufacturing Technology*, vol. 121, no. 9, pp. 5651–5675, 2022.

[24] M. Koltsaki and M. Mavri, "A comprehensive overview of additive manufacturing processes through a time-based classification model," *3D printing and additive manufacturing*, vol. 11, no. 1, pp. 363–382, 2024.

[25] E. Ghinatti, T. Islam, S. Pan, R. Bertolini, and S. Bruschi, "Effect of layer thickness on the microstructure and machinability of alsi7mg processed by laser powder bed fusion," *CIRP Journal of Manufacturing Science and Technology*, vol. 64, pp. 137–148, 2026.

[26] Q. Fang, G. Xiong, F. Wang, Z. Shen, X. Dong, and F.-Y. Wang, "Uncertainty-aware parameter optimization for reliable laser powder bed fusion additive manufacturing," *IEEE Transactions on Automation Science and Engineering*, 2025.

[27] Z. Kazemi, A. Nayebi, H. Rokhgireh, and M. Soleimani, "A multiobjective optimization of laser powder bed fusion process parameters to reduce defects by modified taguchi method," *steel research international*, vol. 96, no. 6, p. 2400628, 2025.

[28] T. Yue, Z. Zou, S. Zhang, H. Liu, Q. Chen, W. Wen, and Y. Zang, "Effects of volumetric energy density on melting modes, printability, microstructures, and mechanical properties of laser powder bed fusion (l-pbf) printed pure nickel," *Materials Science and Engineering: A*, vol. 909, p. 146871, 2024.

[29] Z. Gu, S. Sharma, D. A. Riley, M. V. Pantawane, S. S. Joshi, S. Fu, and N. B. Dahotre, "A universal predictor-based machine learning model for optimal process maps in laser powder bed fusion process," *Journal of Intelligent Manufacturing*, vol. 34, no. 8, pp. 3341–3363, 2023.

[30] V. Trofimov, S. Xu, Z. Dong, G. Hu, Y. Zou, Y. Yang, and C. Han, “Development of a universal multimodal prediction method to optimise process parameters for improving densification during laser powder bed fusion,” *Virtual and Physical Prototyping*, vol. 19, no. 1, p. e2424463, 2024.

[31] Y. Zhang, S. Yang, G. Dong, and Y. F. Zhao, “Predictive manufacturability assessment system for laser powder bed fusion based on a hybrid machine learning model,” *Additive Manufacturing*, vol. 41, p. 101946, 2021.

[32] Q. Zeng, K. Wang, S. Lu, C. Lu, and X. Li, “Modeling and optimization of energy consumption, surface quality and relative density in gh3625 superalloy by laser powder bed melting via rsm mopso and critic-topsis,” *Optics & Laser Technology*, vol. 184, p. 112411, 2025.

[33] I. Gibson, D. Rosen, B. Stucker, M. Khorasani, D. Rosen, B. Stucker, and M. Khorasani, *Additive manufacturing technologies*, vol. 17. Springer, 2021.

[34] D. Herzog, V. Seyda, E. Wycisk, and C. Emmelmann, “Additive manufacturing of metals,” *Acta Materialia*, vol. 117, pp. 371–392, 2016.

[35] Y. Tachibana, T.-T. Ikeshoji, M. Yonehara, and H. Kyogoku, “Optimization of process parameters in laser beam powder bed fusion using surface texture and density of inconel 718,” *Journal of Advanced Mechanical Design, Systems, and Manufacturing*, vol. 16, no. 5, pp. JAMDSM0050–JAMDSM0050, 2022.

[36] T. DebRoy, H. L. Wei, J. S. Zuback, T. Mukherjee, J. W. Elmer, J. O. Milewski, A. M. Beese, A. d. Wilson-Heid, A. De, and W. Zhang, “Additive manufacturing of metallic components–process, structure and properties,” *Progress in materials science*, vol. 92, pp. 112–224, 2018.

[37] S. A. Khairallah, A. T. Anderson, A. Rubenchik, and W. E. King, “Laser powder-bed fusion additive manufacturing: Physics of complex melt flow and formation mechanisms of pores, spatter, and denudation zones,” *Acta Materialia*, vol. 108, pp. 36–45, 2016.

[38] A. Yadollahi, *Mechanical and fatigue properties of additively manufactured metallic materials*. Mississippi State University, 2017.

[39] W. King, A. T. Anderson, R. M. Ferencz, N. E. Hodge, C. Kamath, and S. A. Khairallah, "Overview of modelling and simulation of metal powder bed fusion process at lawrence livermore national laboratory," *Materials Science and Technology*, vol. 31, no. 8, pp. 957–968, 2015.

[40] G. Tapia and A. Elwany, "A review on process monitoring and control in metal-based additive manufacturing," *Journal of Manufacturing Science and Engineering*, vol. 136, no. 6, p. 060801, 2014.

[41] J. Galarza, J. Barron, L. Jimenez, T. Oraby, J. Li, and F. Ahmed, "A machine learning approach to detect pores in laser powder bed fusion additive manufacturing," *Manufacturing Letters*, vol. 44, pp. 985–993, 2025.

[42] Y. Liu, Z. Wu, Q. Wang, L. Zhao, X. Zhang, W. Gao, J. Xu, Y. Song, X. Song, and X. Zhang, "Optimization of parameters in laser powder bed fusion ta15 titanium alloy using taguchi method," *Crystals*, vol. 12, no. 10, p. 1385, 2022.

[43] N. Choudhary and D. Kaur, "Effect of ti addition on the structural, mechanical and damping properties of magnetron sputtered ni–mn–sn ferromagnetic shape memory alloy thin films," *Journal of Physics D: Applied Physics*, vol. 45, no. 49, p. 495304, 2012.

[44] J. Zhou, Y. Lu, Q. Tian, H. Liu, M. Hasanipanah, and J. Huang, "Advanced machine learning methods for prediction of blast-induced flyrock using hybrid svr methods," *Computer Modeling in Engineering & Sciences*, vol. 140, no. 2, p. 1595, 2024.

[45] S. Gorgannejad, A. A. Martin, J. W. Nicolino, M. Strantza, G. M. Guss, S. Khairallah, J.-B. Forien, V. Thampy, S. Liu, P. Quan, *et al.*, "Localized keyhole pore prediction during laser powder bed fusion via multimodal process monitoring and x-ray radiography," *Additive Manufacturing*, vol. 78, p. 103810, 2023.

[46] Q. Zhu, Z. Liu, and J. Yan, "Machine learning for metal additive manufacturing: predicting temperature and melt pool fluid dynamics using physics-informed neural networks," *Computational Mechanics*, vol. 67, no. 2, pp. 619–635, 2021.

[47] J. Qin, F. Hu, Y. Liu, P. Witherell, C. C. Wang, D. W. Rosen, T. W. Simpson, Y. Lu, and Q. Tang, "Research and application of machine learning for additive manufacturing," *Additive Manufacturing*, vol. 52, p. 102691, 2022.

[48] B. Ahmadikia, A. L. Beyerlein, J. M. Hestroffer, M. A. Kumar, and I. J. Beyerlein, "Designing ti-6al-4v microstructure for strain delocalization using neural networks," *Journal of Materials Science: Materials Theory*, vol. 8, no. 1, p. 4, 2024.

[49] E. Maleki and N. Maleki, "Artificial neural network modeling of pt/c cathode degradation in pem fuel cells," *Journal of Electronic Materials*, vol. 45, no. 8, pp. 3822–3834, 2016.

[50] A. S. Mohammed, M. Almutahhar, K. Sattar, A. Alhajeri, A. Nazir, and U. Ali, "Deep learning based porosity prediction for additively manufactured laser powder-bed fusion parts," *Journal of Materials Research and Technology*, vol. 27, pp. 7330–7335, 2023.

[51] N. D. Parab, C. Zhao, R. Cunningham, L. I. Escano, K. Fezzaa, W. Everhart, A. D. Rollett, L. Chen, and T. Sun, "Ultrafast x-ray imaging of laser–metal additive manufacturing processes," *Synchrotron Radiation*, vol. 25, no. 5, pp. 1467–1477, 2018.

[52] N. D. Parab, C. Zhao, R. Cunningham, L. I. Escano, K. Fezzaa, W. Everhart, A. D. Rollett, L. Chen, and T. Sun, "Ultrafast x-ray imaging of laser–metal additive manufacturing processes," *Synchrotron Radiation*, vol. 25, no. 5, pp. 1467–1477, 2018.

[53] S. Theeda, S. H. Jagdale, B. B. Ravichander, and G. Kumar, "Optimization of process parameters in laser powder bed fusion of ss 316l parts using artificial neural networks," *Metals*, vol. 13, no. 5, p. 842, 2023.

[54] H. Baumgartl, J. Tomas, R. Buettner, and M. Merkel, "A deep learning-based model for defect detection in laser-powder bed fusion using in-situ thermographic monitoring," *Progress in Additive Manufacturing*, vol. 5, no. 3, pp. 277–285, 2020.

[55] Y. Zhang, S. Yang, G. Dong, and Y. F. Zhao, "Predictive manufacturability assessment system for laser powder bed fusion based on a hybrid machine learning model," *Additive Manufacturing*, vol. 41, p. 101946, 2021.

[56] T. Herzog, M. Brandt, A. Trinchi, A. Sola, and A. Molotnikov, "Process monitoring and machine learning for defect detection in laser-based metal additive manufacturing," *Journal of Intelligent Manufacturing*, vol. 35, no. 4, pp. 1407–1437, 2024.

[57] S. L. Sing, C. Kuo, C. Shih, C. Ho, and C. K. Chua, "Perspectives of using machine learning in laser powder bed fusion for metal additive manufacturing," *Virtual and Physical Prototyping*, vol. 16, no. 3, pp. 372–386, 2021.

[58] T. Sahar, M. Rauf, A. Murtaza, L. A. Khan, H. Ayub, S. M. Jameel, and I. U. Ahad, "Anomaly detection in laser powder bed fusion using machine learning: A review," *Results in Engineering*, vol. 17, p. 100803, 2023.

[59] J. Liu, J. Ye, D. Silva Izquierdo, A. Vinel, N. Shamsaei, and S. Shao, "A review of machine learning techniques for process and performance optimization in laser beam powder bed fusion additive manufacturing," *Journal of Intelligent Manufacturing*, vol. 34, no. 8, pp. 3249–3275, 2023.

[60] K. Li, R. Ma, Y. Qin, N. Gong, J. Wu, P. Wen, S. Tan, D. Z. Zhang, L. E. Murr, and J. Luo, "A review of the multi-dimensional application of machine learning to improve the integrated intelligence of laser powder bed fusion," *Journal of Materials Processing Technology*, vol. 318, p. 118032, 2023.

[61] A. Moradi Ghasemabadi, *Machine Learning Assisted Laser-Powder Bed Fusion Process Optimization for AISI 316L-Cu Alloy.* PhD thesis, Politecnico di Torino, 2024.

[62] M. A. Obeidi, "Achieving high quality nitinol parts with minimised input thermal energy by optimised pulse wave laser powder bed fusion process," *Results in Materials*, vol. 14, p. 100279, 2022.

Appendix A

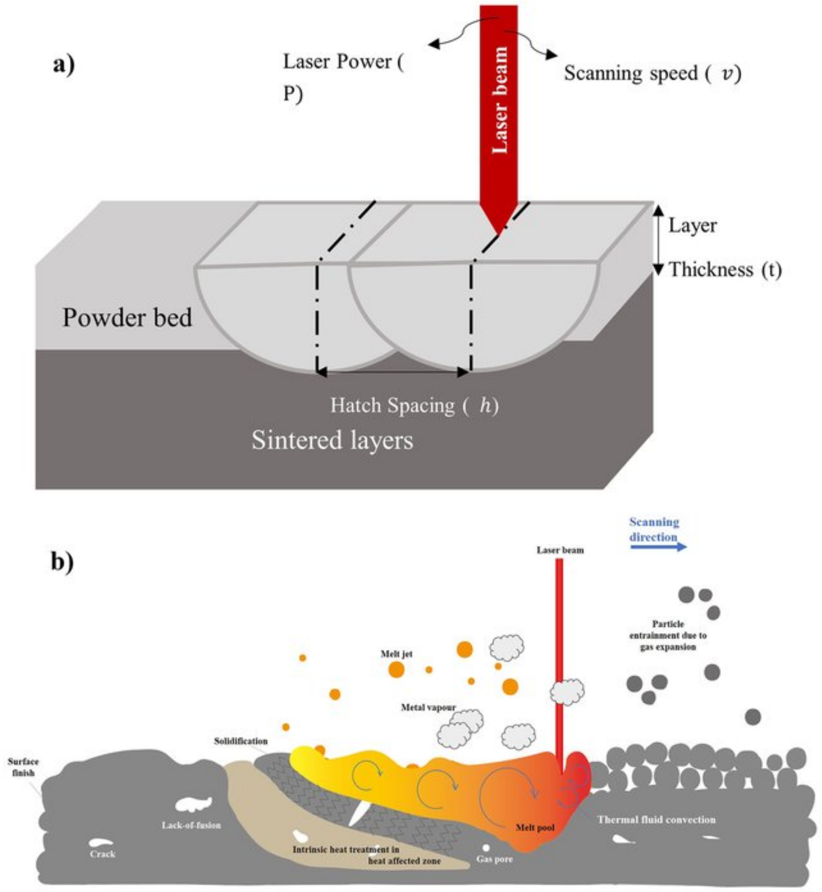

FIGURE A.1: Effect of scanning speed in L-PBF: (a) influence on energy input per unit length, and (b) schematic of melt-pool behaviour and defect formation Source [23]

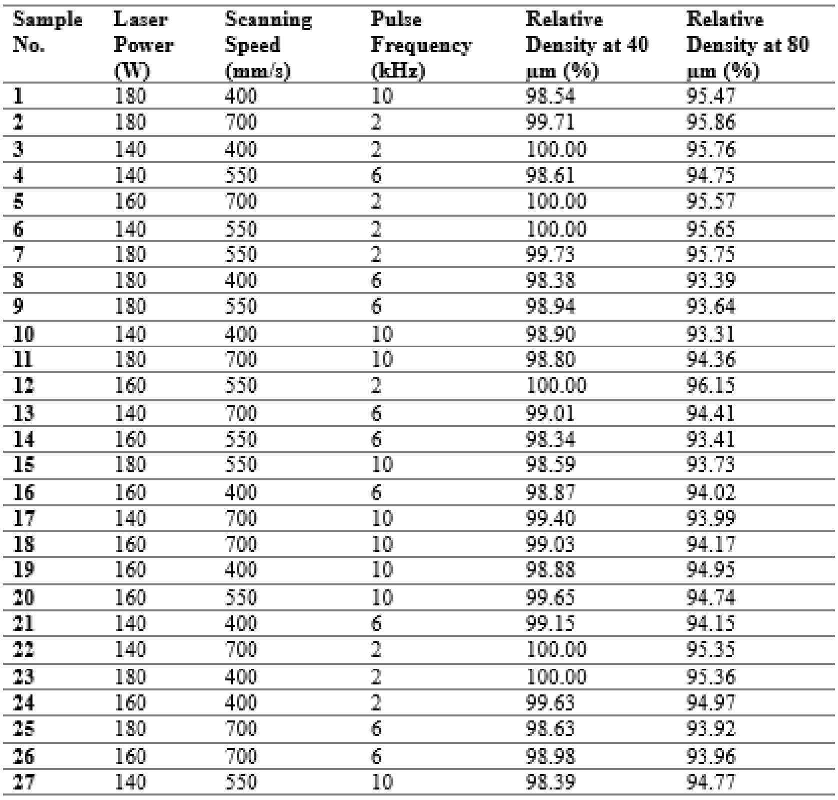

Sample No.	Laser Power (W)	Scanning Speed (mm/s)	Pulse Frequency (kHz)	Relative Density at 40 µm (%)	Relative Density at 80 µm (%)
1	180	400	10	98.54	95.47
2	180	700	2	99.71	95.86
3	140	400	2	100.00	95.76
4	140	550	6	98.61	94.75
5	160	700	2	100.00	95.57
6	140	550	2	100.00	95.65
7	180	550	2	99.73	95.75
8	180	400	6	98.38	93.39
9	180	550	6	98.94	93.64
10	140	400	10	98.90	93.31
11	180	700	10	98.80	94.36
12	160	550	2	100.00	96.15
13	140	700	6	99.01	94.41
14	160	550	6	98.34	93.41
15	180	550	10	98.59	93.73
16	160	400	6	98.87	94.02
17	140	700	10	99.40	93.99
18	160	700	10	99.03	94.17
19	160	400	10	98.88	94.95
20	160	550	10	99.65	94.74
21	140	400	6	99.15	94.15
22	140	700	2	100.00	95.35
23	180	400	2	100.00	95.36
24	160	400	2	99.63	94.97
25	180	700	6	98.63	93.92
26	160	700	6	98.98	93.96
27	140	550	10	98.39	94.77

Appendix B

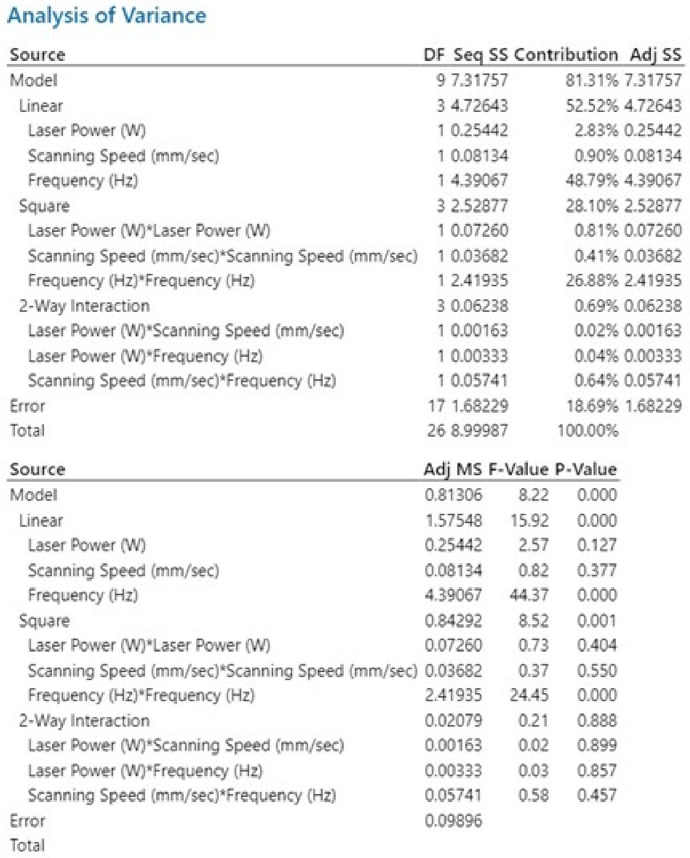

Analysis of Variance

Source	DF	Seq SS	Contribution	Adj SS
Model	9	7.31757	81.31%	7.31757
Linear	3	4.72643	52.52%	4.72643
Laser Power (W)	1	0.25442	2.83%	0.25442
Scanning Speed (mm/sec)	1	0.08134	0.90%	0.08134
Frequency (Hz)	1	4.39067	48.79%	4.39067
Square	3	2.52877	28.10%	2.52877
Laser Power (W)*Laser Power (W)	1	0.07260	0.81%	0.07260
Scanning Speed (mm/sec)*Scanning Speed (mm/sec)	1	0.03682	0.41%	0.03682
Frequency (Hz)*Frequency (Hz)	1	2.41935	26.88%	2.41935
2-Way Interaction	3	0.06238	0.69%	0.06238
Laser Power (W)*Scanning Speed (mm/sec)	1	0.00163	0.02%	0.00163
Laser Power (W)*Frequency (Hz)	1	0.00333	0.04%	0.00333
Scanning Speed (mm/sec)*Frequency (Hz)	1	0.05741	0.64%	0.05741
Error	17	1.68229	18.69%	1.68229
Total	26	8.99987	100.00%	

Source	Adj MS	F-Value	P-Value
Model	0.81306	8.22	0.000
Linear	1.57548	15.92	0.000
Laser Power (W)	0.25442	2.57	0.127
Scanning Speed (mm/sec)	0.08134	0.82	0.377
Frequency (Hz)	4.39067	44.37	0.000
Square	0.84292	8.52	0.001
Laser Power (W)*Laser Power (W)	0.07260	0.73	0.404
Scanning Speed (mm/sec)*Scanning Speed (mm/sec)	0.03682	0.37	0.550
Frequency (Hz)*Frequency (Hz)	2.41935	24.45	0.000
2-Way Interaction	0.02079	0.21	0.888
Laser Power (W)*Scanning Speed (mm/sec)	0.00163	0.02	0.899
Laser Power (W)*Frequency (Hz)	0.00333	0.03	0.857
Scanning Speed (mm/sec)*Frequency (Hz)	0.05741	0.58	0.457
Error	0.09896		
Total			

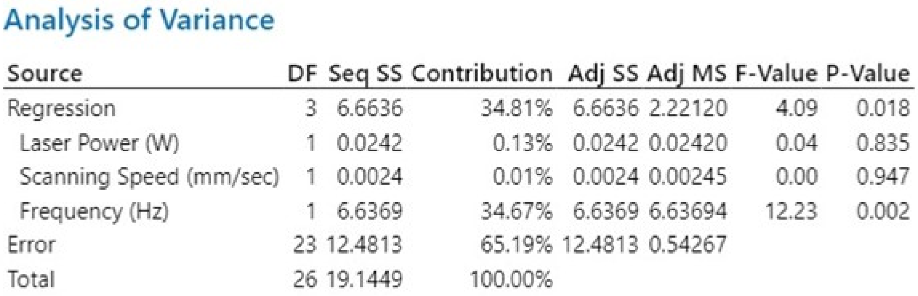

Analysis of Variance

Source	DF	Seq SS	Contribution	Adj SS	Adj MS	F-Value	P-Value
Regression	3	6.6636	34.81%	6.6636	2.22120	4.09	0.018
Laser Power (W)	1	0.0242	0.13%	0.0242	0.02420	0.04	0.835
Scanning Speed (mm/sec)	1	0.0024	0.01%	0.0024	0.00245	0.00	0.947
Frequency (Hz)	1	6.6369	34.67%	6.6369	6.63694	12.23	0.002
Error	23	12.4813	65.19%	12.4813	0.54267		
Total	26	19.1449	100.00%				